JOURNAL OF PETROLOGY | VOLUME 0 | NUMBER 0 | PAGES 1–32 | 2010 | doi:10.1093/petrology/egq066
Journal of Petrology Advance Access published November 23, 2010

Polybaric Fractional Crystallization of High-alumina Basalt Parental Magmas in the Egersund–Ogna Massif-type Anorthosite (Rogaland, SW Norway) Constrained by Plagioclase and High-alumina Orthopyroxene Megacrysts

B. CHARLIER[1]*, J.-C. DUCHESNE[1], J. VANDER AUWERA[1], J.-Y. STORME[1], R. MAQUIL[2] AND J. LONGHI[3]

[1]DEPARTMENT OF GEOLOGY, UNIVERSITY OF LIEGE, B-4000 SART TILMAN, BELGIUM
[2]GEOLOGICAL SURVEY OF GRAND DUCHY OF LUXEMBOURG, L-LUXEMBOURG, LUXEMBOURG
[3]LAMONT–DOHERTY EARTH OBSERVATORY, PALISADES, NY 10964, USA

RECEIVED AUGUST 6, 2009; ACCEPTED OCTOBER 7, 2010

Bulk analyses of plagioclase and high-alumina orthopyroxene megacrysts (decimetre- to metre-sized crystals with plagioclase lamellae) from the late Proterozoic Egersund–Ogna massif-type anorthosite (Rogaland anorthosite province, SW Norway) are used to constrain the parental magma compositions and differentiation processes within this 30 km diameter diapir. Spatial compositional variations show that two types of anorthosite occur: high-Sr (720–1090 ppm) andesine anorthosite ($An_{48\pm4}$) in the centre of the intrusion and low-Sr (320–620 ppm) labradorite anorthosite ($An_{59\pm6}$) in the margin. Two populations of orthopyroxene megacrysts are clearly discriminated by their Mn and Cr contents, but display similar ranges of Mg-number (55–79). Interpretation of trace element data and comparison with inversion models suggest that the two types of anorthosite result from crystallization of different parental magma compositions with high-alumina basalt affinities and similar Mg-numbers, but different wollastonite, Sr, Mn and Cr contents. A Rayleigh fractional crystallization model of the trace element concentrations vs MgO content in orthopyroxene constrains the cotectic orthopyroxene:plagioclase proportions to 0·33:0·67 in both magma types before the appearance of Fe–Ti oxide minerals on the liquidus at F *~0·7 (where* F *is melt fraction). Polybaric crystallization is recorded by variable alumina contents in the orthopyroxene megacrysts (2·3–8·5 wt %), corresponding to crystallization pressures in the 3–13 kbar range as shown by experimental data. This implies that the high-alumina orthopyroxene megacrysts mainly crystallized en route during diapiric rise of the anorthositic mush. Modelling the plagioclase compositions with experimentally determined partition coefficients for Ca, K, Sr and Ba confirms that pressure variation during polybaric crystallization is the main controlling factor on compositional variations in the anorthosite pluton.*

KEY WORDS: *Proterozoic; AMCG; trace element modelling; partition coefficients; emplacement mechanism; diapir*

INTRODUCTION

Classical views on the emplacement of Proterozoic massif-type anorthosites consider that they crystallized in two stages (Kushiro & Fujii, 1977; Emslie, 1985; Longhi & Ashwal, 1985; Ashwal, 1993; Duchesne *et al.*, 1999; Fig. 1). The initial stage involves accumulation of buoyant

*Corresponding author. E-mail: B.Charlier@ulg.ac.be
Present address: Department of Earth, Atmospheric and Planetary Sciences, Massachusetts Institute of Technology, Cambridge, MA 02139, USA

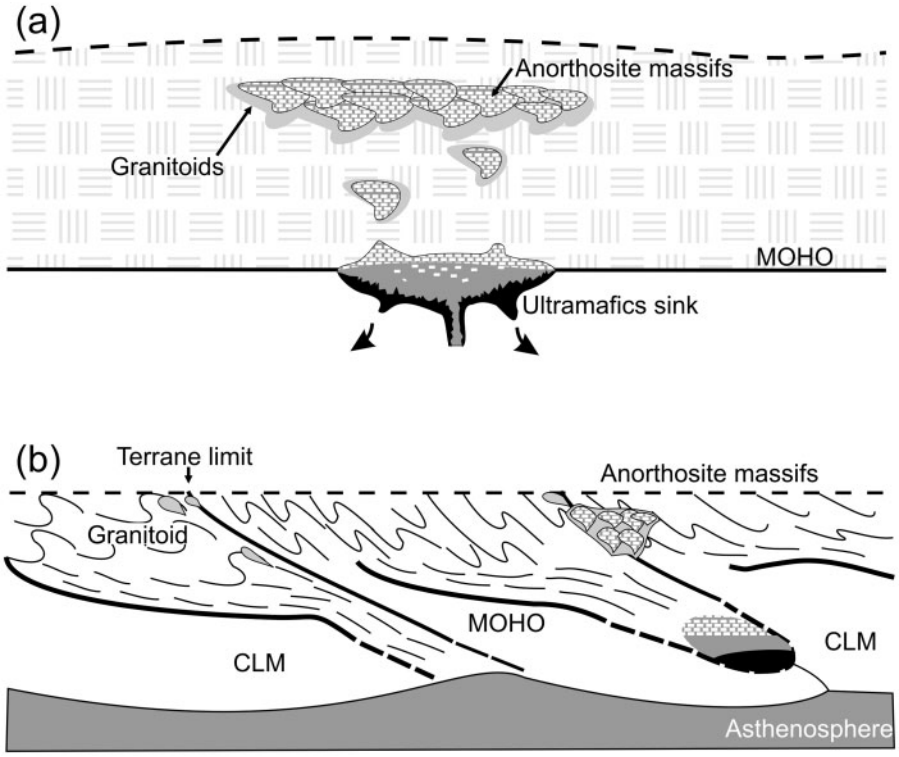

Fig. 1. Proposed models for massif-type anorthosite genesis. (a) Anorogenic two-stage model of Ashwal (1993). Mantle-derived mafic melts pond at the crust–mantle boundary (Moho), where mafic silicates crystallize and sink. Residual melts become enriched in Al and Fe/Mg. Plagioclase is buoyant in these dense melts, producing anorthositic cumulates at the top of the magma chamber. The plagioclase-rich mush is gravitationally unstable, rises through the crust, dragging aggregates of high-alumina orthopyroxene megacrysts in sub-ophitic assemblage with plagioclase. The mush coalesces as plutons at mid-crustal levels. Heat from the crystallizing mantle-derived magma causes crustal anatexis to form granitoid magmas. (b) Post-collisional crustal tongue melting model of Duchesne *et al.* (1999). Collisional stacking of terranes produces: (1) underthrust lower crust tongues; (2) granitic liquids by anatexis of mid-crustal material. These intrude at higher levels along terrane boundaries, as a result of delamination along zones of weakness. Some 10 Myr later the rise in temperature melts a crustal tongue of suitable composition and a deep-seated magma chamber develops in which plagioclase floats to accumulate at the roof. Resultant anorthosite diapirs rise through the crust, channelled by zones of weakness, and coalesce higher up at mid-crustal levels; the mafic cumulates, left behind, become indistinguishable from the mantle. A Moho offset represents the only evidence of the former magma chamber. CLM, continental lithospheric mantle.

plagioclase at the top of deep-seated magma chambers, followed by the intrusion of a low-density plagioclase mush at mid-crustal level as a result of gravitational instability. The ascent of anorthositic mushes by simple vertical diapirism has been successfully modelled (Barnichon *et al.*, 1999); however, the emplacement is probably favoured by pre-existing zones of weakness within the crust (Corrigan & Hanmer, 1997; Scoates & Chamberlain, 1997; Duchesne *et al.*, 1999; Ryan, 2000; Bogdanova *et al.*, 2004; Myers *et al.*, 2008). The polybaric crystallization of anorthosites has been partly deduced from the occurrence of high-alumina orthopyroxene megacrysts (HAOM; Emslie, 1975; Wiebe, 1992). Although some workers have suggested that HAOM result from metastable rapid growth at low pressure (Morse, 1975; Dymek & Gromet, 1984; Xue & Morse, 1994; Owens & Dymek, 1995), experiments on the stability of HAOM reveal that they are stable at pressures in the 11–13 kbar range (Fram & Longhi, 1992; Longhi *et al.*, 1993). These high-alumina orthopyroxene megacrysts are easily distinguished by their characteristic plagioclase lamellae from large orthopyroxene crystals with higher Fe/Mg ratios that occur in pegmatoidal masses that crystallized at the final depth of emplacement from more evolved liquids. The final emplacement pressure of anorthosite crystallization has been estimated from mineral assemblages in contact metamorphic aureoles to be in the range 3–6 kbar (Berg, 1977; Jansen *et al.*, 1985; Wilmart & Duchesne, 1987; Westphal *et al.*, 2003).

Proposed emplacement mechanisms for massif-type anorthosites have not convincingly explained the crystallization history of the rising mush. Were anorthosites emplaced in a two-stage crystallization process or was polybaric crystallization continuous over a large interval of pressure? Based on detailed mapping, large anorthosite bodies are composite in nature (e.g. Harp Lake, Labrador; Emslie, 1980), which may imply emplacement

in multiple pulses. Moreover, the high-pressure cotectic cumulate of magmas parental to anorthosites cannot easily be estimated because of plagioclase sorting that resulted from gravitational instability. The compositions of the parental magmas remain highly debated and are considered either as high-alumina basalt or primitive jotunite, a hypersthene-bearing monzodiorite (e.g. Mitchell *et al.*, 1995; Vander Auwera *et al.*, 1998; Longhi *et al.*, 1999; Bédard, 2001).

In this contribution, we present new data on the compositions of plagioclase and high-alumina orthopyroxene megacrysts (HAOM) from the Egersund–Ogna anorthosite that forms part of the Rogaland anorthosite province in SW Norway. We use the spatial variation of plagioclase and orthopyroxene compositions, as well as modelling of chemical evolution by polybaric Rayleigh crystallization, to understand the emplacement mechanism of this massif-type anorthosite. These results also constrain the composition of plausible parent magmas to the Egersund–Ogna anorthosite.

THE EGERSUND–OGNA MASSIF

Geology and rock types

The 929 ± 2 Ma Egersund–Ogna massif (EGOG; Fig. 2) is an anorthositic dome, *c.* 30 km in diameter with subcontinuous outcrop (Fig. 3a), emplaced into granulite-facies terranes (Michot & Michot, 1969; Schärer *et al.*, 1996). The anorthosite is petrographically homogeneous and comprises recrystallized, equal-sized (1–3 cm) plagioclase grains locally with some megacrysts of orthopyroxene (HAOM) and plagioclase. Detailed mapping (Maquil & Duchesne, 1984; Duchesne & Maquil, 1987), revisited by Marker *et al.* (2003), has distinguished several varieties of anorthosite and leuconorite, forming a more or less concentric structure (Fig. 2). In the central part of the massif (along the coast, near Hellvik), orthopyroxene megacrysts are more abundant than elsewhere, and form metre-sized sub-ophitic aggregates with megacrysts of plagioclase (Fig. 3b). A typical facies, called the anorthositic–noritic complex (Maquil & Duchesne, 1984; Duchesne *et al.*, 1985*b*), is characterized by the occurrence of such aggregates embedded and grossly oriented in a medium-grained leuconoritic to noritic matrix in which the orthopyroxene is markedly different in composition (low Al and Cr contents) from the HAOM. This matrix has been interpreted as a melt laden with aggregates of plagioclase and orthopyroxene megacrysts (Duchesne & Maquil, 1987; Duchesne & Korneliussen, 2003).

The marginal zone of the massif (1–3 km thick; here referred to as the 'margin') is formed by rock types and associations similar to those in the core of the massif (here called the 'centre'), but in various stages of deformation (Fig. 3c–f), which has produced a variety of textures from a simple magmatic orientation to a completely recrystallized granoblastic gneissic texture. The foliation in the leuconoritic margin and in the surrounding gneisses is generally concordant. The degree of deformation varies considerably from place to place giving rise to variable grain sizes, from lenses (augen) of metre-sized crystals down to millimetre-sized grains in gneisses where the HAOM are kinked, recrystallized and locally stretched over several metres along the foliation (Fig. 3c–f). In the deformed anorthositic–noritic complex, the aggregates of plagioclase give rise to layers, bands or lenses of meta-anorthosite, the aggregates of plagioclase and HAOM become coarse-grained leuconoritic gneisses, and the leuconoritic matrix becomes a fine-grained leuconoritic gneiss. Evidence that deformation occurred in several episodes is provided by the occurrence of sharp-walled decimetre-wide dykes of leuconorite cutting across the foliation in the margin, which are locally sheared (and foliated), faulted and displaced a few metres along strike. Blocky enclaves of strongly recrystallized and deformed anorthosite and leuconoritic gneiss (Fig. 3g), metres to decametres long and with sharp contacts with the enclosing rock, can be found at several locations in the central anorthosite (Duchesne & Maquil, 1987; Duchesne & Korneliussen, 2003). Metre-thick Fe–Ti oxide-rich noritic dykes, commonly pegmatitic, occur everywhere in the anorthosite, but are more concentrated towards the margin. Petrographically, they contrast with the leuconoritic material by the presence of Fe–Ti oxide minerals.

A system of large jotunitic dykes tens to hundreds of metres wide cuts across the anorthosites and neighbouring intrusions (Duchesne *et al.*, 1985*a*). These grade in composition from norite to mangerite. Dolerite dykes dated at 616 Ma have been considered to be related to the opening of the Iapetus Ocean (Bingen *et al.*, 1998).

Mechanism of emplacement

Evidence of continuous deformation from the magmatic stage to the solid stage in both the centre and margin of the massif, as well as the ubiquitous dynamic recrystallization of plagioclase (primary crystals are replaced by smaller recrystallized grains; e.g. Lafrance *et al.*, 1996), are typical syn-emplacement features of Proterozoic anorthosites (Martignole & Schrijver, 1970). In the present case, these features are highly suggestive of the diapiric emplacement and associated ballooning of the intrusion as proposed by Duchesne *et al.* (1985*b*) and further supported by finite-element modelling (Barnichon *et al.*, 1999). The depth of final emplacement of the Rogaland anorthosite province has been estimated to ~3–6 kbar (Wilmart & Duchesne, 1987; Vander Auwera & Longhi, 1994). Gravity data (Smithson & Ramberg, 1979) have been used to infer that the present thickness of the anorthosite massif is of the order of 4 km. The intrusion thus appears to be a relatively thin lens, ~30 km in diameter.

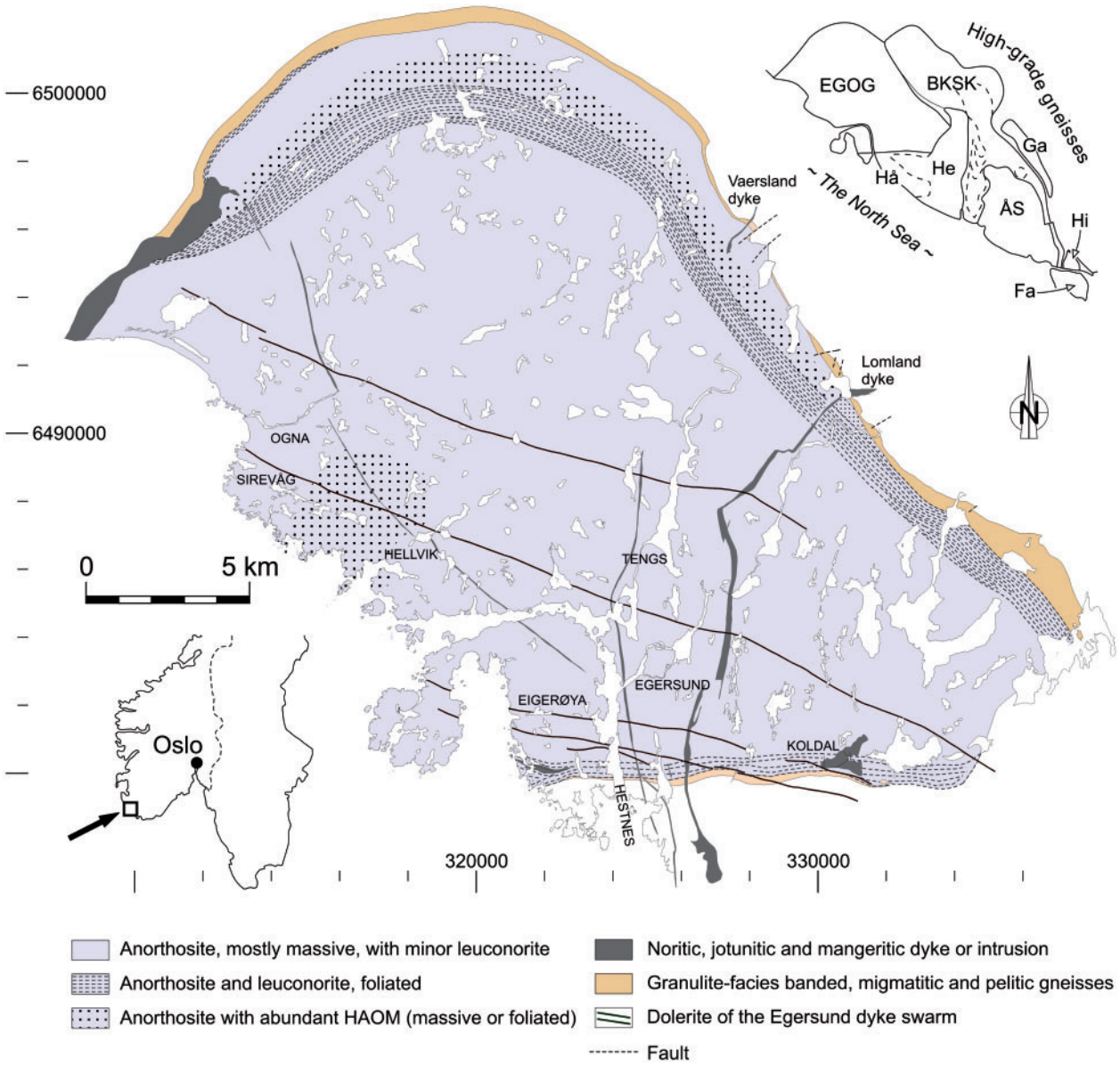

Fig. 2. Geological map of the Egersund–Ogna massif-type anorthosite after Duchesne & Maquil (1987) and Marker *et al.* (2003). Grid is the EUREF89 kilometric UTM. Inset map: EGOG, Egersund–Ogna anorthosite; Hå, Håland anorthosite; He, Helleren anorthosite; ÅS, Åna–Sira anorthosite; Hi, Hidra anorthosite; Ga, Garsaknatt leuconorite; Fa, Farsund charnockite; BKSK, Bjerkreim–Sokndal layered intrusion.

PETROGRAPHY

High-alumina orthopyroxene megacrysts (HAOM)

The HAOM vary from decimetre- to metre-size and are characterized by the presence of plagioclase lamellae. Maquil & Duchesne (1984) showed that the largest plagioclase exsolution lamellae or granules display reverse zoning (An_{65} to An_{72}). Thinner exsolution lamellae are commonly more calcic (An_{77}). Clinopyroxene lamellae, much thinner than the plagioclase lamellae, and granules occur rarely. They have equilibrated with the host orthopyroxene at temperatures in the range 830–990°C (Maquil & Duchesne, 1984). Fe–Ti oxide minerals (hemo-ilmenite, Ti-magnetite) also occur as platelets or rods segmenting the plagioclase lamellae (Fig. 4). Morse (1975) suggested that they are produced by an oxy-exsolution reaction coupled with the exsolution of plagioclase.

HAOM are deformed to various degrees. Moderate deformation is characterized by kink bands. More intense deformation produces complete polygonization and

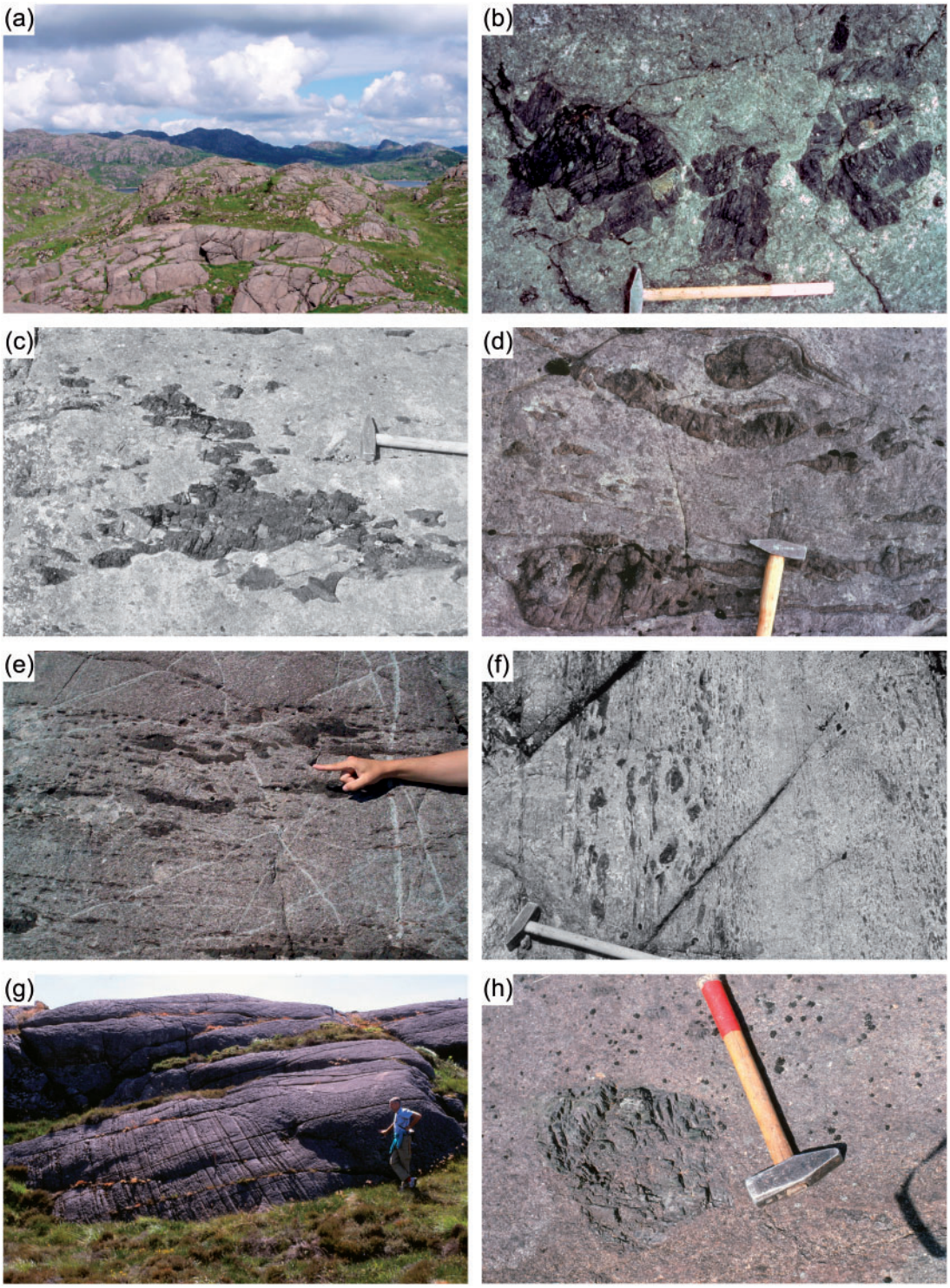

Fig. 3. Photographs of field relationships in the Egersund–Ogna anorthosite. (a) Typical landscape in Rogaland anorthosites with sub-continuous outcrops. Photographs (b)–(f) display high-alumina orthopyroxene megacrysts in anorthosite with increasing degree of deformation, from nearly undeformed (b), oriented aggregates (c), lenses (d), to highly foliated gneissic structure (e) and (f). The hammer handle is 1 m long. In the less deformed aggregates (b), straight contacts between orthopyroxene and plagioclase outline the crystal faces of megacrysts of plagioclase, thus indicating a sub-ophitic texture. (g) Blocky inclusion of anorthositic–leuconoritic gneiss enclosed in a norite. (h) Megacryst of plagioclase, partly granulated, in a medium-grained anorthosite; the hammer is 30 cm long.

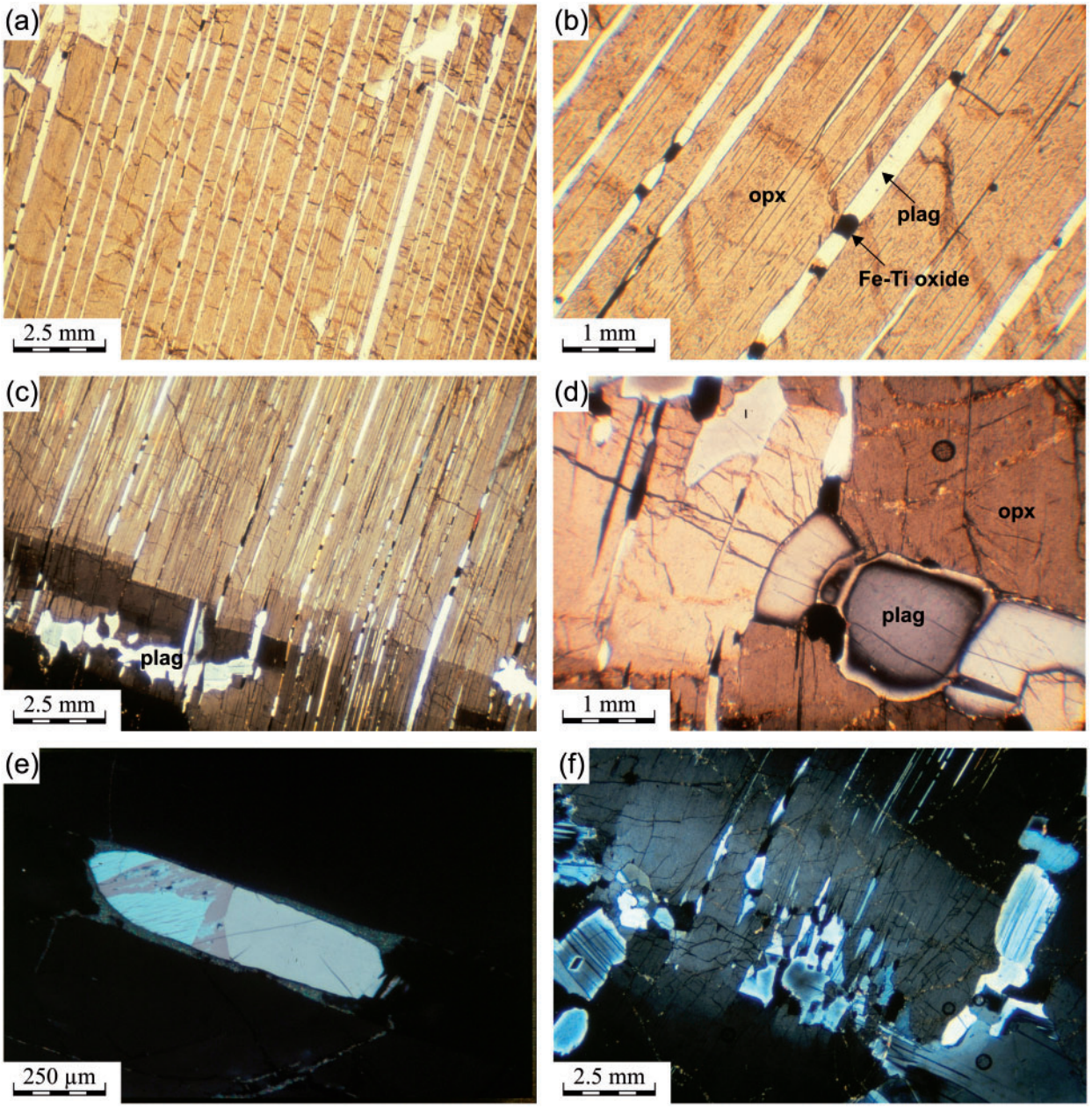

Fig. 4. Photomicrographs of the main textures observed in high-alumina orthopyroxene in the Egersund–Ogna anorthosite. (a) Plagioclase lamellae in orthopyroxene, parallel to the (l00) planes of orthopyroxene and from 0·2 mm to 1 mm apart; (b) Detail of plagioclase lamellae in orthopyroxene, up to 25 µm wide and segmented by platelets of Fe–Ti oxides; (c) kinked orthopyroxene megacryst with concentration of plagioclase granules formed by stress-induced exsolution; some granules are in continuity with plagioclase lamellae; (d) plagioclase granules displaying strong inverse zoning (the core of the grain is more sodic than the rim in contact with the orthopyroxene) in a mosaic of recrystallized grains of orthopyroxene; (e) platelet of Fe–Ti oxide mineral made up of a homogeneous magnetite grain (right part of the grain) in contact with a hemo-ilmenite grain (left part); the exsolution lamellae in the two coarse hematite lenses and thin hematite lamellae (partly altered to leucoxene) in the host ilmenite should be noted; (f) granules of plagioclase in a deformed part of an orthopyroxene.

recrystallization of the pyroxene, and the exsolved plagioclase forms granules within the pyroxene grain mosaic (Fig. 4c, d and f). It is commonly observed that these plagioclase granules have migrated outside the deformed pyroxene grain and form a corona around the pyroxene. The HAOM, commonly in sub-ophitic association with plagioclase megacrysts, are contained in medium-grained leuconorite, in which the orthopyroxene is much lower in

Al and Cr content and does not contain plagioclase lamellae.

Plagioclase

Two types of plagioclase can be defined in the field, megacrysts and matrix plagioclase, the latter being the most common type in anorthosite and leuconorite. Matrix plagioclases vary in colour from pink to blue and they are locally iridescent. They commonly exhibit a xenomorphic, roughly equigranular texture. The megacrysts are rare and occur alone (Fig. 3h) or associated with HAOM. They are always deformed and partly recrystallized, even in the less deformed part of the intrusion. When they coexist with HAOM, their idiomorphic primary shape can be defined by straight contacts with HAOM, the latter being less recrystallized (Fig. 3b). The predominant colour of the megacrysts is grey; blue or pink megacrysts are less abundant. Some megacrysts in the centre of the intrusion are typically iridescent with a range of blue–green colours, which suggests a weak zoning from *c.* An_{52} to An_{53} (Smith & Ribbe, 1969). In the marginal facies, the megacrysts are porphyroclasts preserved from the extensive deformation, which has elsewhere drastically reduced the grain size and promoted a granoblastic texture. Petrographically, the megacrysts show 'dust-like' Fe–Ti oxide inclusions. In general, exsolution lamellae are less abundant in recrystallized grains, a typical feature of most massif-type anorthosites (Ashwal, 1993).

Other minerals

Olivine (Fo_{70}) is locally present in some meta-leuconorites in the margin. Hemo-ilmenite is a very rare trace mineral, but is somewhat more common in the most central part of the body. Clinopyroxene is absent, except as exsolution lamellae in HAOM. Several occurrences of Fe–Cu–Ni sulphides have been described by Schiellerup *et al.* (2003), commonly disseminated in noritic and orthopyroxenitic cumulates and also present as small massive ore bodies. These sulphides are dominated by pyrrhotite, chalcopyrite, pentlandite and pyrite. Zircon and baddeleyite are rare but have been extracted from HAOM aggregates for geochronology (Schärer *et al.*, 1996).

SAMPLING AND ANALYTICAL METHODS

The HAOM samples were collected in the intrusion (Fig. 5a) with hammer and chisel when possible or with a saw on flat outcrops. In the margin, only undeformed parts of large porphyroclasts were considered for sampling to avoid the change in composition owing to external granule exsolution of plagioclase. For the study of plagioclase, a total of 212 rock samples were collected, including 52 porphyroclasts from the margin and 81 megacrysts from the centre (Fig. 5b). The megacrysts were simply crushed on a

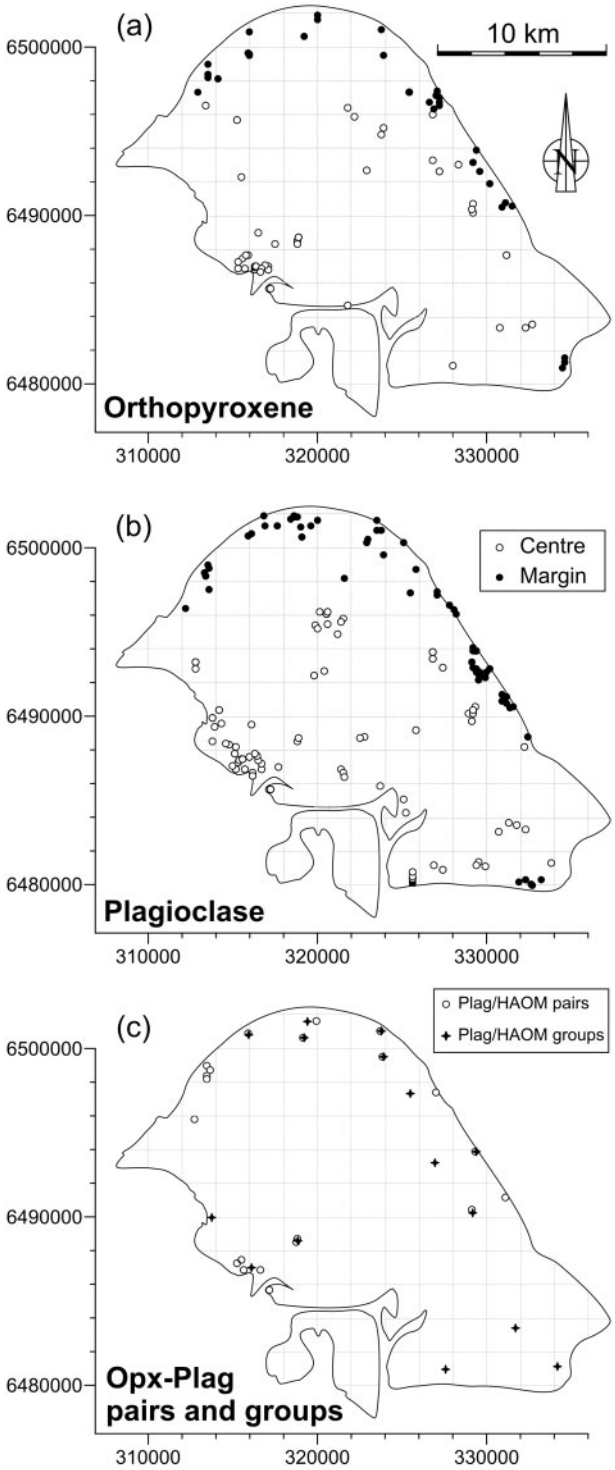

Fig. 5. Sample locations for (a) orthopyroxene, (b) plagioclase and (c) orthopyroxene–plagioclase pairs and groups. Grid is the EUREF89 kilometric UTM.

steel anvil and powdered in agate ball mill jars. The matrix plagioclase grains from both anorthosites and leuconorites were separated using bromoform and purified with a Frantz magnetic separator before being powdered and analysed.

Several plagioclase megacrysts and HAOM were sampled from the same sub-ophitic aggregate (Fig. 5c). They thus constitute 21 pairs of minerals probably formed at the same P–T conditions, which is an important constraint in the interpretation of their origin. This sampling method permits an estimate of the natural compositional heterogeneity of the samples together with the analytical precision. We have also considered 17 groups of samples consisting of plagioclase from neighbouring localities and HAOM from the same area within the EGOG anorthosite.

Plagioclase was analysed as pressed powder pellets for Ca, K, Sr, Ba, Fe and Ti by X-ray fluorescence (XRF) on a CGR Lamda 2020 spectrometer (from 1977 to 1999) and on an ARL 9400XP (from 2000). The matrix effect on Sr determinations was monitored by the Compton scattered tube line. Bulk HAOM compositions (orthopyroxene + exsolved phases) were analysed for major elements (Si, Ti, Al, Fe, Mn, Mg, Ca, Na, K) by XRF on lithium-borate fused glass discs and for trace elements (Zn, Ni, Co, Cu, V, Cr, Zr) on pressed powder pellets. The Compton scattered tube line was used for matrix effects on Zn, Ni, Co, Cu and Zr. The matrix influence on V and Cr was neglected, because of the relatively small compositional range of the mineral. All orthopyroxene analyses were performed using an ARL 9400XP spectrometer.

MINERAL COMPOSITIONS

Geochemistry of HAOM

One hundred HAOM (52 in the centre and 48 in the margin) were analysed for major oxides and trace element concentrations (data are available as Supplementary Data 1, at http://petrology.oxfordjournals.org/). Spatial variations of orthopyroxene compositions for Mg-number, Al_2O_3 and Cr are illustrated in Fig. 6. The HAOM from the centre have the highest Al_2O_3 (*c.* 8–8·5 wt %) with Mg-number = 76–78 (Mg-number = 100[MgO/(MgO + FeO_t)] mol %) and grade towards lower Al_2O_3 contents (2·5 wt %) and Mg-number (58). Most margin HAOM cluster between 3 and 6 wt % Al_2O_3. They also show a general decrease of Al content with Mg-number, the latter varying in a similar range to HAOM from the central part of the intrusion (Mg-number = 58–79; Fig. 7).

The correlation of trace elements in HAOM with Mg-number is illustrated in Fig. 7. The Cr concentrations in the less evolved HAOM from the central part vary between 800 and 1500 ppm and decrease to 300 ppm at Mg-number = 58. In contrast, the Cr concentrations in the margin HAOM increase from 1100 ppm at Mg-number = 77 to 2000 ppm for Mg-number = 73, then abruptly decrease to 1000 ppm at Mg-number = 70, then smoothly to 500 ppm at Mg-number = 58. Several samples

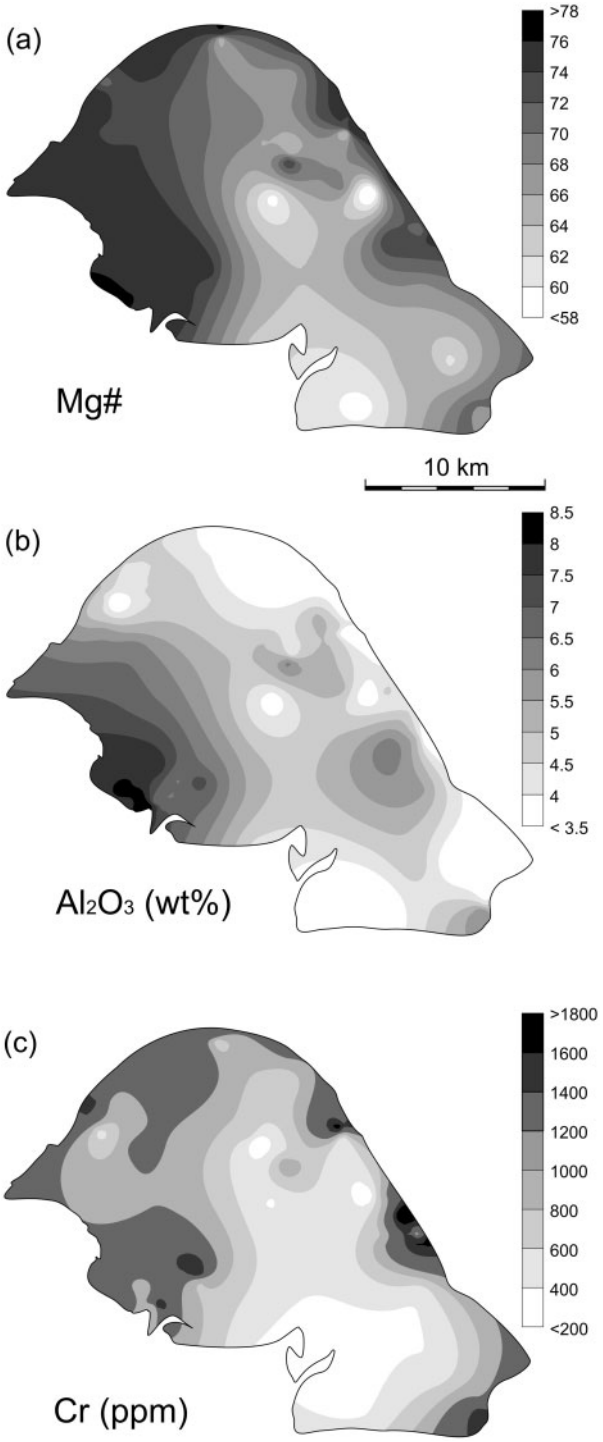

Fig. 6. Spatial variations of Mg-number, Al_2O_3 and Cr in orthopyroxene using the point kriging method.

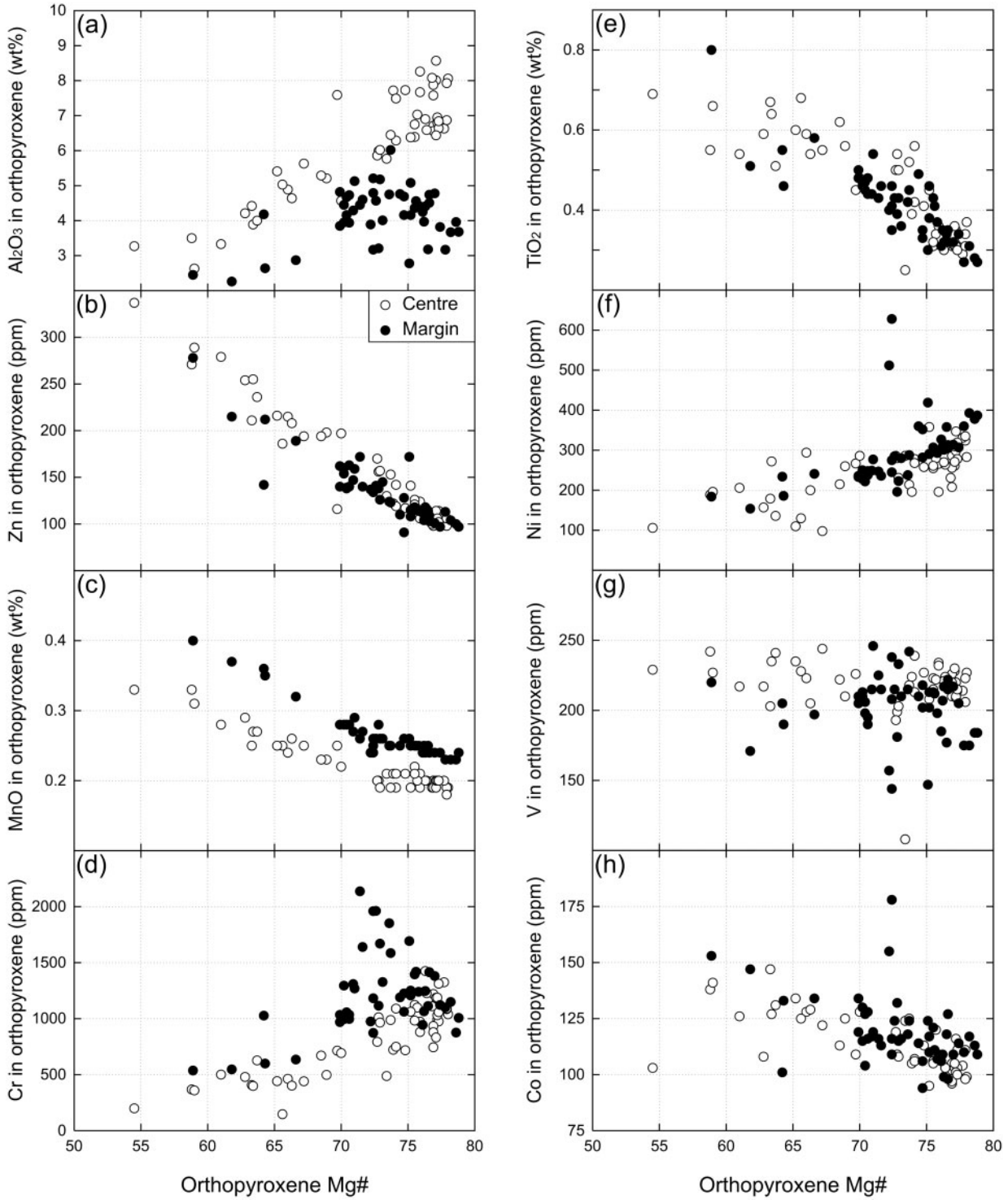

Fig. 7. Orthopyroxene composition showing the variation of Al_2O_3, Zn, MnO, Cr, TiO_2, Ni, V and Co as a function of Mg-number.

collected in the same aggregate of minerals show a relatively large dispersion in Cr (18 rel. %) compared with Mg-number (1·5 rel. %) or Al content (6·5 rel. %), which suggests possible zoning of Cr in the megacrysts.

HAOM from the centre and margin differ with respect to their MnO concentrations, which show parallel evolutionary trends with Mg-number (enrichment factor of 1·6); these are higher by 0·05 wt % (500 ppm) in the

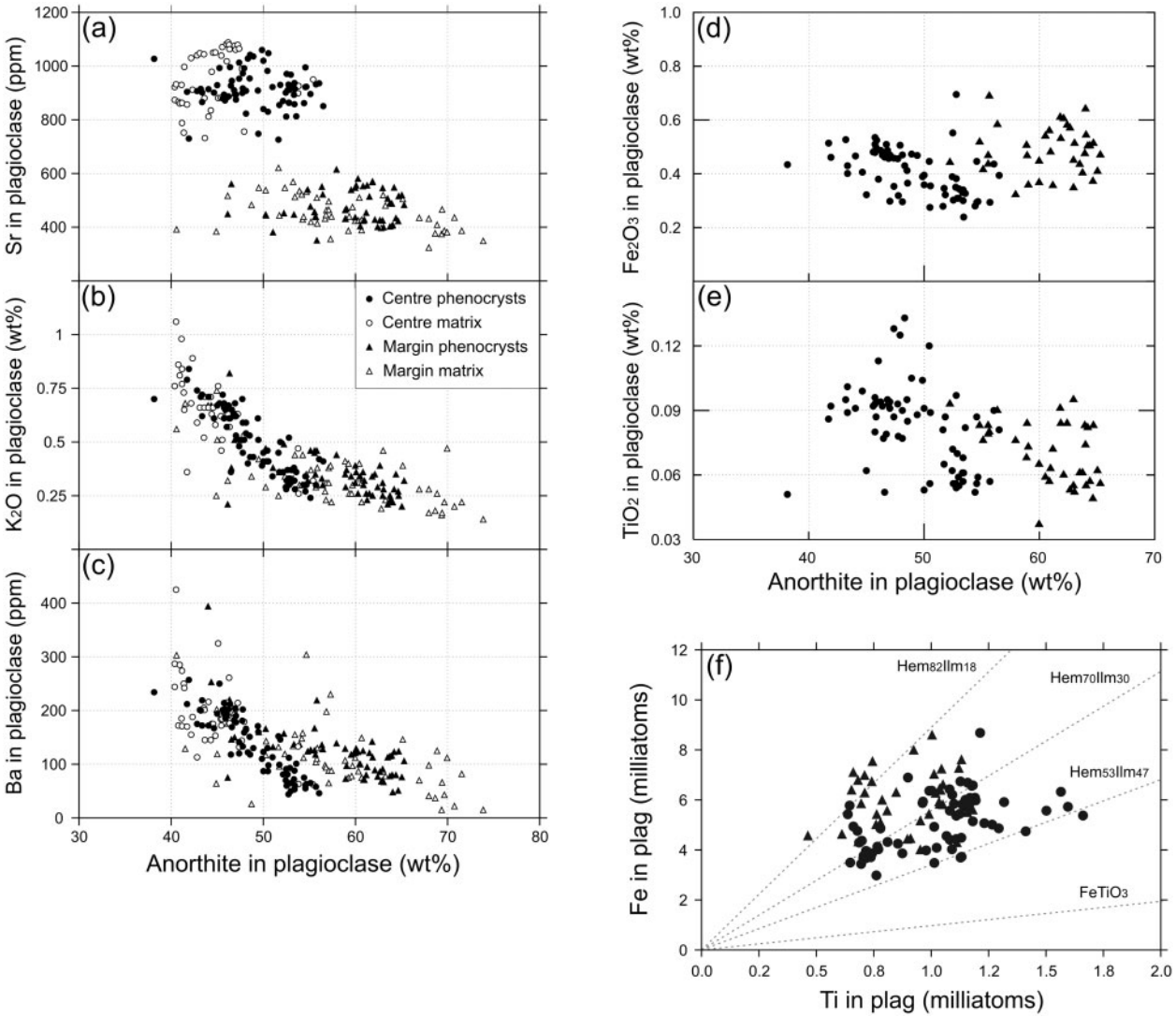

Fig. 8. (a–e) Plagioclase composition showing the variation of Sr, K_2O, Ba, Fe_2O_3 and TiO_2 as a function of anorthite content and (f) Fe vs Ti (milliatoms) in plagioclase megacrysts.

margin. Ti, Zn, Ni, Co, and V are similar in the centre and margin HAOM. Ti and Zn concentrations are highly correlated with Mg-number, exhibiting enrichment factors of 2·0 and 2·7, respectively. Co and Ni are more dispersed (possibly as a result of local contamination by sulphides) and show opposite trends, with Ni decreasing and Co increasing with decreasing Mg-number. Vanadium shows some erratic values but remains grossly constant with variation in Mg-number, the average value being 211 ±22 ppm. Zr exhibits less well-defined trends (not shown), possibly owing to inclusions of zircon (Schärer *et al.*, 1996).

Geochemistry of plagioclase

We use the geochemistry of 220 plagioclase samples, including 126 megacrysts, analysed for Ca, K, Sr, Ba, Ti, and Fe (Supplementary Data 2). We calculate the weight per cent of anorthite as CaO × 4·961 and neglect the other element contents (MgO < 0·2 wt %, Fe_2O_3 < 0·6 wt %, TiO_2 < 0·1 wt %). In the andesine–labradorite compositional range, the calculated An value is close to the molar An. The small difference between the weight per cent and the mol per cent does not affect the interpretation. Plagioclase from the central part and the margin show contrasting compositions (Fig. 8). In the central part of the EGOG, the An content (wt %) of the plagioclase varies between An_{38} and An_{57} (average An_{48}, andesine) with an average Sr concentration of 926 ± 84 ppm. In the margin, the An content ranges from An_{40} to An_{74} (average An_{59}, labradorite) and the Sr concentration averages 462 ± 68 ppm. This is illustrated by the spatial variations of plagioclase composition for An and Sr (Fig. 9). Ba and

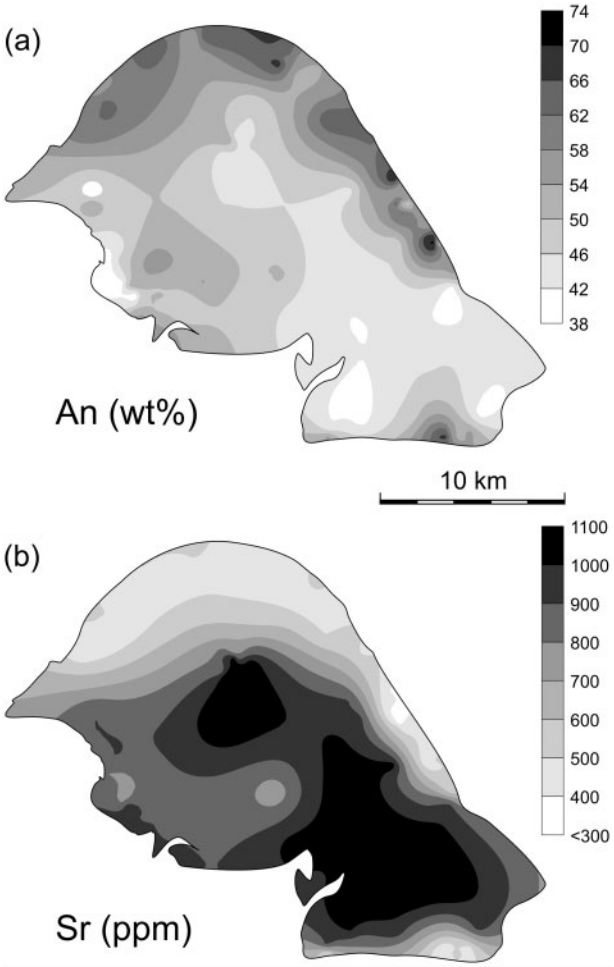

Fig. 9. Spatial variations of anorthite (wt %) and Sr (ppm) in plagioclase using the point kriging method.

K_2O steadily increase with decreasing An content in plagioclase from the centre (megacrysts and matrix) by factors of four and 2·7, respectively (Fig. 8). These elements also increase in the margin plagioclase with enrichment factors of 3·4 and 5·3, respectively. There is no significant difference in K_2O and Ba concentrations at similar An contents between the margin and centre plagioclase.

TiO_2 and Fe_2O_3 were measured only on megacrysts to avoid the effects of recrystallization and/or the systematic bias owing to magnetic separation, which removes the Fe-rich grains. Average values of Fe_2O_3 and TiO_2 are similar: $0{\cdot}48 \pm 0{\cdot}09$ wt % and $0{\cdot}07 \pm 0{\cdot}01$ wt % respectively in the margin, and $0{\cdot}41 \pm 0{\cdot}09$ wt % and $0{\cdot}08 \pm 0{\cdot}02$ wt % respectively in the centre. Both elements show insignificant variation with An content (Fig. 8d and e). Some information on the nature of the dust-like Fe–Ti oxide inclusions can be obtained from the relationship between Fe and Ti (Fig. 8f). The Fe–Ti ratio of the average plagioclase points to an ilmeno-hematite composition ($Hem_{70}Ilm_{30}$) and the margin plagioclase has on average a higher Fe/Ti ratio than the centre plagioclase. This would possibly indicate higher fO_2 conditions of crystallization in the margin than in the centre.

Pairs of plagioclase and HAOM

Compositions of pairs of minerals and average compositions of groups are provided in Table 1. These data (Fig. 10) show that (1) in the central part of the EGOG, HAOM vary from 8·5 to 4 wt % Al_2O_3 and are associated with andesine plagioclase with high Sr concentrations (925 ppm), and (2) in the margin, low-Sr (450 ppm) labradorite coexists with HAOM, which vary from 3 to 6 wt % Al_2O_3 (Fig. 10). At equivalent Mg-number or Al_2O_3 contents of the HAOM, the coexisting plagioclase is 10–15 mol % more albitic in the centre than in the margin (Fig. 10). In detail, for orthopyroxene Mg-number >75, the An values in the centre vary from An_{44} to An_{55} and cluster at *c.* An_{53} and *c.* An_{45}. The range of Mg-number of orthopyroxene in the margin and in the centre is similar.

Plagioclase from enclaves

Plagioclase compositions from anorthosite enclaves sampled in the centre of the EGOG intrusion are given in Table 2 and their Sr–An relationship is compared with plagioclase from the centre and margin of the massif in Fig. 11. Most plagioclase from the enclaves has a margin signature, with low-Sr concentrations and labradorite compositions, which suggests that the enclaves are blocky fragments of margin rocks that have been enclosed in the central part of the intrusion (Duchesne & Maquil, 1987). This observation is important for deciphering the mechanism of the emplacement of the EGOG body and will be revisited in the discussion.

DISCUSSION

Chasing the magma compositions

Plagioclase compositions are more Ca-rich in the margin than in the centre, where andesine to labradorite dominate. There are no intermediate sample compositions, indicating a continuity of Sr concentrations in plagioclase between the margin and centre samples, and the HAOM from the centre and margin are distinctly different in their Mn concentrations. The Cr concentrations in the HAOM from the margin are also much higher than those in the centre. These features strongly suggest that the rocks forming the centre and the margin of the EGOG massif crystallized from different magmas.

In the Harp Lake complex, Labrador, Emslie (1980) identified a large number of possible parental melts that have an average high-alumina basalt composition, which has been studied experimentally by Longhi and his

Table 1: Composition of plagioclase and high-alumina orthopyroxene megacrysts from the same outcrop or the same area

Longitude:	3122	3294	3271	3312	3161	3133	3134	3239	3237	3200
Latitude:	64964	64939	64973	64912	65008	64985	64983	64996	65010	65016
Plagioclase	RM 77-16-3	RM77-66m	RM77-74m	RM 77-8-3	RM 78-118	RM79-10m	RM79-11m	RM 79-159-2	RM79-160m	RM 79-197-2
n:	1	2	2	1	1	4	4	1	2	1
An wt %	60·33	64·02	63·58	63·25	63·75	58·75	61·12	52·24	61·64	64·64
CaO %	12·16	12·91	12·82	12·75	12·85	11·84	12·32	10·53	12·43	13·03
K_2O %	0·33	0·22	0·27	0·23	0·23	0·39	0·33	0·49	0·35	0·27
Sr ppm	425	408	547	481	490	494	421	452	449	423
Ba ppm	87	64	107	78	115	114	83	157	105	51
Fe_2O_3 %		0·59	0·48			0·53	0·55	0·44	0·50	0·37
TiO_2 %		0·064	0·088			0·070	0·060	0·093	0·062	0·049

HAOM	RM77-16-7	RM77-66-13-3	RM77-74-4	RM77-8m	RM78-118	RM79-10-1	RM79-11-1	RM79-159-1	RM79-160-1a	RM79-197-1
n:	1	1	1	2	1	1	1	1	1	1
Major elements (%)										
SiO_2	51·08	52·15	52·89	51·26	52·42	52·04	51·63	50·17	51·97	49·79
TiO_2	0·42	0·31	0·34	0·45	0·33	0·32	0·35	0·58	0·39	0·46
Al_2O_3	5·78	4·25	3·18	4·57	4·69	4·41	4·74	2·87	3·21	2·64
Fe_2O_{3tot}	16·92	15·72	15·65	18·21	15·98	15·39	15·60	21·78	17·98	22·99
MnO	0·25	0·24	0·25	0·27	0·26	0·24	0·24	0·32	0·28	0·35
MgO	24·43	25·24	25·70	23·15	23·85	25·03	25·78	21·91	24·33	20·93
CaO	1·49	2·40	2·05	2·08	2·23	1·89	1·68	2·11	1·80	2·00
Na_2O	0·00	0·00	0·00	0·00	0·05	0·02	0·00	0·00	0·00	0·00
K_2O	0·27	0·06	0·00	0·16	0·01	0·15	0·19	0·00	0·01	0·02
P_2O_5	0·00	0·00	0·00	0·00	0·00	0·01	0·00	0·00	0·00	0·00
Total	100·64	100·37	100·06	100·14	99·82	99·50	100·21	99·74	99·97	99·18
Trace elements (ppm)										
Co	98	106	118	123	94	99	127	134	132	133
Cr	1456	944	1113	1333	1226	1247	1414	635	1116	599
Ni	320	327	358	226	352	301	305	241	196	186
V	247	185	177	223	202	217	215	197	181	190
Zn	133	112	114	140	91	118	103	189	138	212
Zr	14	14	25	15	10	21	9·1	18	15	15
Cations/6O										
Si	1·798	1·836	1·863	1·821	1·851	1·843	1·819	1·813	1·846	1·816
Ti	0·011	0·008	0·009	0·012	0·009	0·009	0·009	0·016	0·010	0·013
Al	0·240	0·176	0·132	0·191	0·195	0·184	0·197	0·122	0·134	0·113
Fe_{tot}	0·448	0·416	0·415	0·487	0·425	0·410	0·414	0·592	0·481	0·631
Mn	0·007	0·007	0·007	0·008	0·008	0·007	0·007	0·010	0·008	0·011
Mg	1·281	1·324	1·350	1·226	1·256	1·322	1·354	1·180	1·288	1·138
Ca	0·056	0·091	0·077	0·079	0·084	0·072	0·063	0·082	0·068	0·078
Na	0·000	0·000	0·000	0·000	0·003	0·001	0·000	0·000	0·000	0·000
K	0·012	0·003	0·000	0·007	0·000	0·007	0·009	0·000	0·000	0·001
Total	3·854	3·861	3·854	3·831	3·832	3·855	3·871	3·814	3·837	3·800
Mg-no.	74·1	76·1	76·5	71·6	74·7	76·3	76·6	66·6	72·8	64·3
En	71·8	72·3	73·3	68·4	71·2	73·3	73·9	63·6	70·1	61·6
Fs	25·1	22·7	22·5	27·2	24·1	22·7	22·6	31·9	26·2	34·2
Wo	3·1	4·9	4·2	4·4	4·8	4·0	3·5	4·4	3·7	4·2

(continued)

Table 1: Continued

Longitude:	3191	3135	3136	3156	3291	3153	3157	3188	3189	3167
Latitude:	65006	64990	64988	64875	64903	64873	64869	64885	64887	64869
Plagioclase	RM79-198m	RM 79-6-2	RM 79-7-2	JCD 75-09-1	RM77-12m	RM 77-59-1	RM77-84m	RM 78-13	RM 78-14-2	RM78-31m
n:	3	1	1	1	4	1	2	1	1	2
An wt %	57·30	55·56	59·98	55·41	48·62	45·00	52·76	54·42	52·79	50·25
CaO %	11·55	11·20	12·09	11·17	9·80	9·07	10·64	10·97	10·64	10·13
K_2O %	0·41	0·46	0·39	0·32	0·43	0·67	0·32	0·30	0·30	0·41
Sr ppm	463	457	437	950	1034	929	970	862	863	835
Ba ppm	112	167	126	62	121	194	55	75	112	87
Fe_2O_3 %	0·40	0·47	0·45		0·41	0·32	0·31	0·28	0·69	0·34
TiO_2 %	0·076	0·083	0·065		0·107	0·062	0·058	0·052	0·097	0·054

HAOM	RM79-198m	RM79-6	RM79-7-1	JCD66-119	RM77-12m	RM77-59-2	RM77-84m	RM78-13m	RM78-14m	RM78-31-1
n:	2	1	1	1	3	1	2	2	2	1
Major elements (%)										
SiO_2	50·83	49·91	50·07	49·79	50·48	50·48	50·09	50·24	50·87	50·88
TiO_2	0·45	0·54	0·86	0·33	0·51	0·37	0·37	0·34	0·36	0·30
Al_2O_3	4·45	5·13	5·51	8·26	6·11	8·06	8·41	7·18	7·19	6·90
Fe_2O_{3tot}	18·57	18·97	19·64	15·42	17·22	14·22	14·82	15·50	15·39	15·40
MnO	0·27	0·29	0·23	0·19	0·19	0·19	0·20	0·21	0·21	0·20
MgO	23·24	23·39	22·31	24·51	23·58	25·42	24·62	24·57	24·70	25·05
CaO	1·94	0·92	1·37	1·47	1·52	1·52	1·89	1·66	1·68	1·39
Na_2O	0·00	0·00	0·00	0·09	0·01	0·00	0·08	0·02	0·06	0·03
K_2O	0·06	0·41	0·08	0·02	0·07	0·08	0·04	0·01	0·02	0·03
P_2O_5	0·00	0·00	0·00	0·00	0·00	0·01	0·01	0·00	0·01	0·00
Total	99·79	99·56	100·07	100·08	99·70	100·35	100·50	99·71	100·46	100·18
Trace elements (ppm)										
Co	115	119	128	109	117	99	100	105	108	99
Cr	1475	1269	849	973	915	1039	791	1024	1015	1425
Ni	243	277	226	266	244	283	308	264	268	270
V	215	246	223	234	205	227	230	219	221	221
Zn	144	159	183	124	160	103	101	115	116	111
Zr	13	18	45	8·9	20	13	14	15	12	14
Cations/6O										
Si	1·814	1·788	1·785	1·753	1·793	1·766	1·754	1·776	1·783	1·787
Ti	0·012	0·015	0·023	0·009	0·014	0·010	0·010	0·009	0·009	0·008
Al	0·187	0·217	0·232	0·343	0·256	0·332	0·347	0·299	0·297	0·286
Fe_{tot}	0·499	0·511	0·527	0·408	0·460	0·374	0·391	0·412	0·406	0·407
Mn	0·008	0·009	0·007	0·006	0·006	0·006	0·006	0·006	0·006	0·006
Mg	1·236	1·249	1·185	1·286	1·248	1·325	1·285	1·294	1·290	1·311
Ca	0·074	0·035	0·052	0·055	0·058	0·057	0·071	0·063	0·063	0·052
Na	0·000	0·000	0·000	0·006	0·001	0·000	0·005	0·001	0·004	0·002
K	0·003	0·019	0·004	0·001	0·003	0·004	0·002	0·000	0·001	0·001
Total	3·833	3·843	3·815	3·867	3·838	3·873	3·871	3·861	3·859	3·860
Mg-no.	71·3	70·9	69·2	75·9	73·1	78·0	76·7	75·8	76·1	76·3
En	68·3	69·6	67·2	73·5	70·7	75·4	73·6	73·1	73·4	74·1
Fs	27·6	28·5	29·9	23·3	26·0	21·3	22·4	23·3	23·1	23·0
Wo	4·1	2·0	3·0	3·2	3·3	3·2	4·1	3·6	3·6	3·0

(continued)

Table 1: Continued

Longitude:	3172	3134	3160	3183	3191	3239	3236	3255	3277	3296
Latitude:	64857	64984	65007	65013	65006	64996	65012	64973	64967	64927
Plagioclase	RM78-78m	B1	B2	B3	B4	B5	B6	B7	B8	B11
n:	8	10	3	2	3	1	1	3	6	17
An wt %	52·23	59·91	63·81	62·73	56·57	52·24	62·86	60·15	62·54	56·01
CaO %	10·53	12·08	12·86	12·65	11·40	10·53	12·67	12·13	12·61	11·29
K_2O %	0·39	0·35	0·23	0·29	0·43	0·49	0·34	0·38	0·27	0·39
Sr ppm	878	446	460	401	467	452	460	463	497	430
Ba ppm	105	104	103	72	116	157	105	136	100	205
Fe_2O_3 %	0·37	0·52	0·44	0·55	0·40	0·44	0·49		0·46	
TiO_2 %	0·071	0·066	0·072	0·068	0·076	0·093	0·060		0·080	

Orthopyroxene	RM78-78-5	B1	B2	B3	B4	B5	B6	B7	B8	B11
n:	1	7	1	1	2	1	1	1	10	11
Major elements (%)										
SiO_2	50·24	50·33	52·42	52·89	50·83	50·17	51·97	52·79	51·70	50·83
TiO_2	0·34	0·45	0·33	0·31	0·45	0·58	0·39	0·41	0·41	0·49
Al_2O_3	7·03	4·52	4·69	3·67	4·45	2·87	3·21	5·21	3·91	4·24
Fe_2O_{3tot}	15·74	17·76	15·98	14·47	18·57	21·78	17·98	16·81	17·79	19·91
MnO	0·20	0·25	0·26	0·23	0·27	0·32	0·28	0·25	0·27	0·28
MgO	24·70	24·92	23·85	26·27	23·24	21·91	24·33	22·28	24·29	21·97
CaO	1·64	1·57	2·23	2·15	1·94	2·11	1·80	1·89	1·58	2·15
Na_2O	0·04	0·01	0·05	0·00	0·00	0·00	0·00	0·09	0·00	0·10
K_2O	0·02	0·15	0·01	0·00	0·06	0·00	0·01	0·07	0·09	0·13
P_2O_5	0·00	0·01	0·00	0·00	0·00	0·00	0·00	0·00	0·00	0·00
Total	99·95	99·97	99·82	99·99	99·79	99·74	99·97	99·80	100·03	100·10
Trace elements (ppm)										
Co	120	131	94	117	115	134	132	109	118	116
Cr	1099	1144	1226	1149	1475	635	1116	1182	1178	1054
Ni	280	366	352	393	243	241	196	245	289	233
V	222	203	202	175	215	197	181	208	204	211
Zn	116	134	91	104	144	189	138	137	146	171
Zr	16	18	10	14	13	18	15	64	14	14
Cations/6O										
Si	1·773	1·792	1·851	1·859	1·814	1·813	1·846	1·864	1·833	1·817
Ti	0·009	0·012	0·009	0·008	0·012	0·016	0·010	0·011	0·011	0·013
Al	0·292	0·190	0·195	0·152	0·187	0·122	0·134	0·217	0·163	0·178
Fe_{tot}	0·418	0·476	0·425	0·383	0·499	0·592	0·481	0·447	0·476	0·537
Mn	0·006	0·007	0·008	0·007	0·008	0·010	0·008	0·007	0·008	0·009
Mg	1·300	1·323	1·256	1·376	1·236	1·180	1·288	1·172	1·283	1·170
Ca	0·062	0·060	0·084	0·081	0·074	0·082	0·068	0·071	0·060	0·082
Na	0·003	0·001	0·003	0·000	0·000	0·000	0·000	0·006	0·000	0·007
K	0·001	0·007	0·000	0·000	0·003	0·000	0·000	0·003	0·004	0·006
Total	3·864	3·867	3·832	3·866	3·832	3·814	3·837	3·798	3·838	3·819
Mg-no.	75·7	73·5	74·7	78·2	71·3	66·6	72·8	72·4	72·9	68·5
En	73·0	71·2	71·2	74·8	68·3	63·6	70·1	69·4	70·5	65·4
Fs	23·5	25·6	24·1	20·8	27·6	31·9	26·2	26·4	26·2	30·0
Wo	3·5	3·2	4·8	4·4	4·1	4·4	3·7	4·2	3·3	4·6

(continued)

Table 1: Continued

Longitude:	3293	3161	3315	3189	3140	3268	3291	3338	3272
Latitude:	64939	64870	64835	64886	64900	64936	64901	64813	64811
Plagioclase	B12	C1	C2	C3	C4	CB9	CB10	CB14	CB15
n:	13	38	4	2	9	7	7	1	2
An wt %	57·71	50·35	46·78	53·60	43·69	46·55	47·95	40·38	41·18
CaO %	11·63	10·15	9·43	10·81	8·81	9·38	9·67	8·14	8·30
K_2O %	0·31	0·46	0·64	0·30	0·69	0·54	0·45	0·76	0·73
Sr ppm	439	903	1059	863	847	920	993	922	929
Ba ppm	122	115	206	94	171	167	132	287	264
Fe_2O_3 %	0·56	0·39		0·49	0·45	0·38	0·39		
TiO_2 %	0·077	0·074		0·074	0·091	0·100	0·104		

Orthopyroxene	B12	C1	C2	C3	C4	CB9	CB10	CB14	CB15
n:	1	20	3	3	1	3	3	4	2
Major elements (%)									
SiO_2	52·15	50·48	50·35	50·25	51·29	50·62	50·48	50·40	50·63
TiO_2	0·31	0·34	0·59	0·37	0·31	0·55	0·51	0·51	0·50
Al_2O_3	4·25	7·26	4·04	7·28	3·68	5·02	6·11	5·20	4·14
Fe_2O_{3tot}	15·72	15·01	22·87	15·81	19·99	19·62	17·22	18·42	21·98
MnO	0·24	0·20	0·26	0·21	0·29	0·23	0·19	0·26	0·28
MgO	25·24	25·16	20·04	24·30	22·58	22·18	23·58	23·15	21·04
CaO	2·40	1·60	1·71	1·67	2·05	1·61	1·52	1·73	1·13
Na_2O	0·00	0·03	0·10	0·03	0·00	0·09	0·01	0·01	0·05
K_2O	0·06	0·03	0·09	0·01	0·00	0·04	0·07	0·06	0·12
P_2O_5	0·00	0·00	0·00	0·00	0·00	0·00	0·00	0·00	0·00
Total	100·37	100·11	100·05	99·92	100·19	99·96	99·70	99·73	99·84
Trace elements (ppm)									
Co	106	104	127	105	119	122	117	124	135
Cr	944	1006	454	932	715	621	915	1220	581
Ni	327	289	257	265	175	254	244	312	173
V	185	221	225	226	215	213	205	221	187
Zn	112	107	250	116	183	196	160	152	219
Zr	14	11	24	16	19	30	20	20	25
Cations/6O									
Si	1·836	1·775	1·813	1·774	1·829	1·806	1·793	1·798	1·819
Ti	0·008	0·009	0·016	0·010	0·008	0·015	0·014	0·014	0·013
Al	0·176	0·301	0·171	0·303	0·155	0·211	0·256	0·219	0·174
Fe_{tot}	0·416	0·397	0·620	0·420	0·537	0·527	0·460	0·495	0·595
Mn	0·007	0·006	0·008	0·006	0·009	0·007	0·006	0·008	0·008
Mg	1·324	1·318	1·075	1·279	1·200	1·179	1·248	1·231	1·125
Ca	0·091	0·060	0·066	0·063	0·078	0·061	0·058	0·066	0·044
Na	0·000	0·002	0·007	0·002	0·000	0·006	0·000	0·001	0·003
K	0·003	0·001	0·004	0·000	0·000	0·002	0·003	0·003	0·005
Total	3·861	3·869	3·781	3·856	3·817	3·814	3·838	3·833	3·787
Mg-no.	76·1	76·9	63·5	75·2	69·1	69·1	73·1	71·3	65·3
En	72·3	74·2	61·1	72·6	66·1	66·7	70·7	68·7	63·8
Fs	22·7	22·4	35·2	23·8	29·6	29·8	26·0	27·6	33·8
Wo	4·9	3·4	3·7	3·6	4·3	3·5	3·3	3·7	2·5

co-workers (HLCA, Harp Lake complex anorthosite, Table 3). In the Rogaland anorthosite province, parental melt compositions are dominated by jotunite, particularly evolved jotunitic melts *sensu* Vander Auwera *et al.* (1998). Primitive jotunites are less abundant, but occur as chilled margins in the Hidra body and Bjerkreim–Sokndal layered intrusion (Demaiffe & Hertogen, 1981; Duchesne & Hertogen, 1988; Robins *et al.*, 1997). In Rogaland, high-alumina basaltic melts are scarce, but present, particularly as a very fine-grained gabbronoritic dyke cutting across the EGOG margin at Saglandsvatn (SG, Table 3). This dyke has a composition similar to HLCA with low $[La/Yb]_N = 2{\cdot}9$ and a small positive Eu anomaly (1·2).

On the basis of experimental work on HLCA (Fram & Longhi, 1992; Longhi *et al.*, 1999), the parental magma of the EGOG margin can be considered to be a high-alumina basalt. At 10–11·5 kbar and dry conditions, HLCA crystallizes HAOM with Mg-number in the 75–77 range, slightly lower than the HAOM in the EGOG margin (Mg-number = 79), and plagioclase in the $An_{54–60}$ range, compatible with the labradoritic compositions in the margin.

Longhi *et al.* (1999) suggested that the parental magma of the central part could be a primitive jotunite similar to the parental melt of the Bjerkreim–Sokndal layered intrusion and slightly more magnesian than TJ (Tjörn), a chill identified by Duchesne & Hertogen (1988) and studied experimentally by Vander Auwera & Longhi (1994). However, TJ at 10–13 kbar crystallizes plagioclase with $An_{41–45}$ and HAOM with a distinctly lower Mg-number (61–67) than the observed value (79). TJ has also a Cr content (28 ppm) too low to be in equilibrium with a HAOM with 1400 ppm Cr. This would imply a D_{Cr}^{opx} of 50, much higher than the value of 14 determined experimentally at high pressure (Vander Auwera *et al.*, 2000); thus TJ is not a likely parental magma composition to the central andesine anorthosite.

We tested the hypothesis of Longhi *et al.* (1999) that a magma slightly more magnesian than TJ could be parental to the central anorthosite and performed backward modelling of the TJ composition. Use of the MELTS algorithm (Ghiorso & Sack, 1995) to assess the liquidus assemblage of TJ was unsuccessful, as the model yielded results far from those observed in the experiments. We therefore calculated an approximation of the backward liquid line of descent by adding to the TJ melt composition increments of solid made up of the most magnesian HAOM (RM77-59-2, Table 1) combined with plagioclase RM77-59-1 (Table 1) in cotectic proportions ($X^{opx} = 0{\cdot}24$). The composition of the liquidus orthopyroxene crystallizing at each step was obtained using the D_{MgO}^{opx} value (5·0) experimentally determined by Vander Auwera & Longhi (1994) and Longhi *et al.* (1999), which is invariant with pressure. The iteration was ended when the melt crystallized an orthopyroxene with the MgO content of RM77-59-2, the fraction of solid added being 0·39. Although the model is a rough estimate, it shows that the calculated initial melt keeps the characteristically high values of TiO_2 (2·3 wt %), K_2O (0·85 wt %) and P_2O_5 of the TJ primitive jotunite. This calculated melt would thus be in equilibrium with a plagioclase richer in these minor elements than the plagioclase formed in the high-alumina basaltic magma of the EGOG margin. However, we observe plagioclase with similar TiO_2 and K_2O in the centre and margin of EGOG. We thus conclude that the parental magma of the centre was not a magnesian primitive jotunite but a high-alumina basalt with an Mg-number similar to HLCA. However, it differs from HLCA by its lower Cr, MnO, CaO and higher Sr.

We further note that plagioclases coexisting with HAOM of high Al content and high Mg-number from the central anorthosite appear to cluster around An_{53} with two values at about An_{45} (Fig. 10). We are thus forced to envisage the hypothesis that two different magma 'pulses' with similar compositions, apart from their CaO contents, could have yielded the two groups of central plagioclase. The CaO contents of these two centre magmas are not constrained by experimental work nor by chilled lithologies, but we show below that geochemical modelling of plagioclase compositions is consistent with this hypothesis.

Modelling the evolution of the high-Al orthopyroxene megacrysts

Al-in-orthopyroxene as a geobarometer

As shown experimentally by Fram & Longhi (1992) and further developed by Longhi *et al.* (1993, 1999), the alumina content of HAOM in equilibrium with plagioclase is a function of pressure and can thus be used as a geobarometer. Pressure vs $^{IV}Al + {}^{VI}Al$ in the HAOM based on available experimental data were compiled by Emslie *et al.* (1994). We use here their empirical relationship P (kbar) $(\pm 0{\cdot}4) = -8{\cdot}2\ (\pm 1{\cdot}0) + 34{\cdot}4\ (\pm 2{\cdot}52) \cdot (^{IV}Al + {}^{VI}Al)^{0{\cdot}5}$, which is fitted to the data of Fram & Longhi (1992) and Longhi *et al.* (1993). The frequency of the apparent pressure of crystallization recorded by HAOM in the centre and margin is shown on the histogram of Fig. 12.

In his pioneering studies, Emslie (1975, 1980) distinguished two types of HAOM: the first type with high alumina contents was inferred to crystallize in a deep-seated magma chamber, the second with low alumina contents, at the level of final emplacement. Our results, however, indicate a continuous variation in the pressure of formation correlated with Al_2O_3 variations. Some 10% of the centre HAOM started crystallizing at 12 kbar (=43 km), *c.* 60% of the population crystallized between 9 and 12 kbar (=32–36 km) and the rest down to 5 kbar (=18 km).

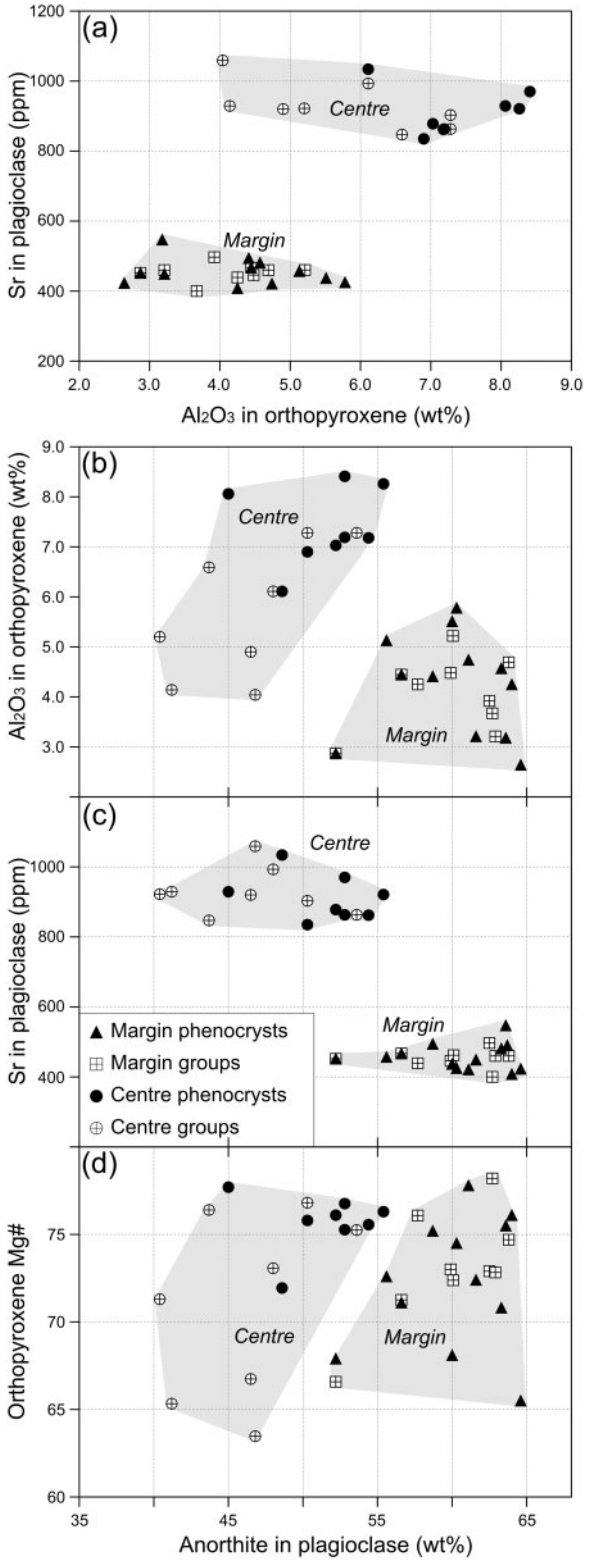

Fig. 10. Compositions of pairs and groups of high-alumina orthopyroxene and plagioclase. The shaded fields indicate the plagioclase and orthopyroxene composition from centre and margin of the EGOG intrusion. It should be noted that (d) shows two groups of plagioclase coexisting with orthopyroxene with Mg-number >75: the first group around An_{45} and the second around An_{53}. These plagioclases have crystallized at pressures of around 10–12 kbar, as indicated in (b) by the Al_2O_3 contents between 7 and 8 wt % in the associated orthopyroxene.

Table 2: Composition of plagioclase from enclaves in the centre of the EGOG intrusion

Sample	An	CaO (%)	Sr (ppm)	K_2O (%)	Ba (ppm)
JCD 66-114	60·5	12·20	414	0·23	77
JCD 66-244	50·6	10·20	660	0·48	85
JCD 66-248	57·1	11·50	479	0·32	85
JCD 66-249	57·1	11·50	469	0·30	98
RM 77-33	50·3	10·14	648	0·33	183
RM 78-124	63·7	12·84	492	0·24	121
RM 78-62-3	45·4	9·15	880	0·58	183
RM 78-62-3′	57·9	11·67	449	0·39	128
RM 79-101-1	57·5	11·60	568	0·41	130
RM 79-101-2	45·9	9·26	903	0·62	178
RM 79-21	58·6	11·82	468	0·35	108
RM 79-23-2	54·3	10·94	553	0·40	140

An is calculated as CaO × 4·961.

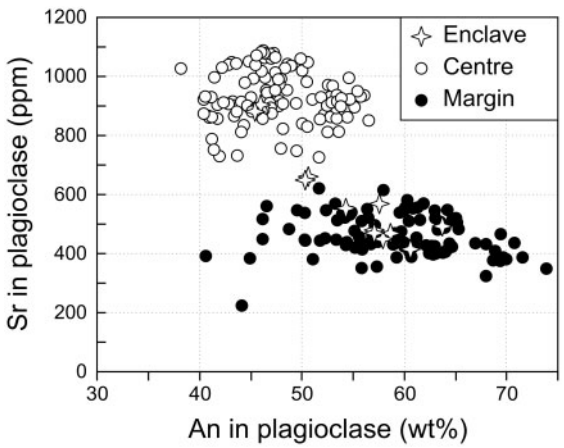

Fig. 11. Sr content in plagioclase as a function of anorthite content in enclaves compared with matrix and megacryst plagioclase from the centre and margin of the Egersund–Ogna anorthosite.

It thus appears that in the diapiric emplacement of a plagioclase crystal–liquid mush, the HAOM mainly crystallized en route during the rise of the mush.

In the margin, the highest alumina concentrations in the HAOM indicate crystallization pressures up to 9 kbar. About 60% of the HAOM from the margin crystallized between 6 and 8 kbar, thus indicating that a large proportion of the magma crystallized at intermediate pressures, possibly in a magma chamber situated at a depth between 21 and 28 km, before rising diapirically and continuing to crystallize en route to the final level of emplacement.

Table 3: Chemical composition of possible parental magmas of the EGOG anorthosite

	High-Al basalt HLCA[1]	High-Al gabbros, mean[2]	JCD79-14 SG[3]	Mt Lister[4]	Primitive jotunite TJ[5]	Evolved jotunite 89.115[6]
SiO_2	50·02	50·29	50·23	49·45	49·70	46·45
TiO_2	1·85	1·82	1·28	1·10	3·63	3·98
Al_2O_3	17·51	17·44	16·20	17·35	15·78	13·22
Fe_2O_{3t}	12·19	11·90	12·10	11·99	12·87	15·72
MnO	0·15	0·18	0·18	0·18	0·15	0·24
MgO	6·67	6·32	7·24	7·76	4·44	3·30
CaO	8·78	8·64	8·86	9·40	6·81	7·81
Na_2O	2·93	2·96	3·36	2·45	3·88	3·54
K_2O	0·44	0·48	0·36	0·42	1·05	1·79
P_2O_5	0·16	0·14	0·19	0·12	0·64	2·35
Total	100·70	100·17	100·00		98·95	98·40
Mg/(Mg + Fe)	0·52	0·51	0·54	0·56	0·41	0·29
U			<0·2		<0·2	
Th			<0·25		0·5	
Zr		20 (25)	93	87	262	253
Hf			3		6·5	5·2
Ta			0·2		1·31	1·71
Sc			30	26	13·8	
Rb			<20	7	18	10·6
Sr		421 (32)	210	370	530	465
Ba		188 (76)	204	158	470	1602
Ni		44 (38)	71	78	60	
V			249	185	216	109
Cr		185 (65)	74	43	28	
Zn		93 (17)	99	81	144	214
Co			52	47	49	48·9
Y			24	18	22	64
La			11·6	23	23·9	65·3
Ce			24·2	48	58	130
Nd			12·9	22	39	92·1
Sm			3·25	4	8·5	21·7
Eu			1·35	1·4	2·86	7·93
Gd			3·1	4·2		18·6
Tb			0·62		1·13	2·69
Yb			2·61	2·2	2	3·49
Lu			0·48		0·33	0·48
$(La/Yb)_n$			2·9	6·8	7·2	13
Eu/Eu*			1·21	1·05	1·05	1·15
*D*CaO plag/melt[7]	1·53[8]	1·46[8]	1·37[8]	1·44[8]	1·34[9]	1·19[9]

[1]Synthetic composition from Fram & Longhi (1992).
[2]Average of 16 analyses from the Harp Lake complex (Emslie, 1980).
[3]Very fine-grained noritic dyke in the EGOG margin (J.-C. Duchesne, unpublished data).
[4]Average of two basic intruding Mt. Lister anorthosite (Emslie *et al.*, 1994, table 7).
[5]Average of two analyses (Duchesne & Hertogen, 1988).
[6]From Vander Auwera *et al.* (1998).
[7]Calculated with the model of Putirka (2005).
[8]At 10 kbar and 1275°C.
[9]At 13 kbar and 1187°C.

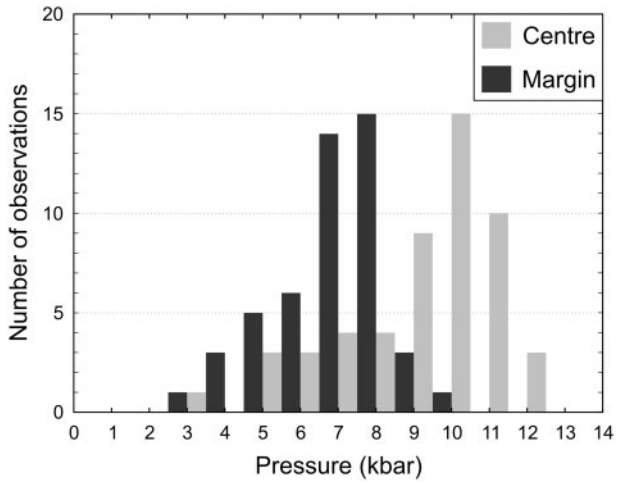

Fig. 12. Histograms of the distribution of pressure calculated from high-alumina orthopyroxene composition in the centre and margin of EGOG using the equation of Emslie *et al.* (1994).

Trace element modelling

Compositions of HAOM from the centre and margin of the EGOG anorthosite are plotted in log–log variation diagrams in Fig. 13. The data define straight lines for Zn and Co in the margin and centre occurrences. The Mn trend is less well defined in the centre than in the margin, but straight lines are acceptable in both cases. Ni is more dispersed in the centre, but a linear relationship is evident, particularly for the most Mg-rich samples. TiO_2 and V in both the margin and centre can reasonably be accounted for by a succession of two straight lines, and for TiO_2 in the centre the Mg-rich line fits the evolution very well. Cr is in general more dispersed in Mg-rich samples, but an overall linear decrease can roughly describe the trend towards more evolved samples.

The linear trends in log–log coordinates indicate that fractional crystallization was the predominant differentiation mechanism (Fig. 13). A forward model can thus be calculated on the basis of the Rayleigh law $C_i^{\mathrm{liq}} = C_i^0 F^{(D_i^{\mathrm{bulk}}-1)}$ in which C_i^0 is the initial concentration of element i in the melt, C_i^{liq} the concentration of i when the system is at a melt fraction F, D_i^{bulk} is the bulk partition coefficient, a constant equal to $\sum X^j \cdot D_i^j$, in which X^j is the corresponding cotectic proportion of the mineral j in the crystallizing assemblage and D_i^j is the mineral j/melt partition coefficient for the element i. Using $D_i^{j/\mathrm{liq}} = C_i^j / C_i^{\mathrm{liq}}$, the Rayleigh law for liquid can be applied to mineral j: $C_i^j = D_i^j \cdot C_i^0 \cdot F^{(D_i^{\mathrm{bulk}}-1)}$. It is worthwhile recalling that a linear trend in log–log coordinates implies a constant value of the bulk partition coefficient D_i^{bulk}. Provided the D_i^j values are known, the slope of the straight line in a log–log diagram, where the concentration of an element is plotted against MgO, depends on the cotectic proportions (the X^j values) of the crystallizing assemblage, which here refers to the proportion of orthopyroxene to plagioclase. Considering that D_i^{plag} values for MgO, TiO_2, Mn, Zn, Co, Ni, V and Cr are negligible, the slope of the trends depends only on D_i^{opx} and X^{opx} and is equal to $(D_{i1}^{\mathrm{opx}} X^{\mathrm{opx}} - 1)/(D_{i2}^{\mathrm{opx}} X^{\mathrm{opx}} - 1)$.

As a proxy for $D_{\mathrm{MgO}}^{\mathrm{opx}}$, we use the $\mathrm{MgO}^{\mathrm{opx}}/\mathrm{MgO}^{\mathrm{melt}}$ ratios experimentally determined on the HLCA composition by Fram & Longhi (1992) and Longhi *et al.* (1999). The $D_{\mathrm{MgO}}^{\mathrm{opx}}$ values obtained at various pressure (from 5 to 13 kbar) and at temperatures close to the liquidus are plotted in Fig. 14. The variation of $D_{\mathrm{MgO}}^{\mathrm{opx}}$ is almost insensitive to pressure variations and can thus be neglected in the modelling; fractionation of HAOM appears to be mainly controlled by temperature. A $D_{\mathrm{MgO}}^{\mathrm{opx}}$ value of 4·1 is adopted here for the centre and margin melts. We also use the $D_{\mathrm{TiO_2}}^{\mathrm{opx}}$ ($0{\cdot}22 \pm 0{\cdot}06$) and $D_{\mathrm{MnO}}^{\mathrm{opx}}$ ($1{\cdot}11 \pm 0{\cdot}23$) obtained in the same experiments. The system is overdetermined because X^{opx} must satisfy two different relationships (TiO_2 vs MgO and MnO vs MgO). It is thus solved by trial and error, the position of the straight line in log–log diagrams being adjusted to the observed trends. A value of $X^{\mathrm{opx}} = 0{\cdot}33$ is obtained as well as $D_{\mathrm{TiO_2}}^{\mathrm{opx}} = 0 \cdot 22$, $D_{\mathrm{MnO}}^{\mathrm{opx}} = 1 \cdot 3$ and the D_i^{opx} values of the other elements (Table 4). In both the margin and centre, we obtain the same X^{opx} and it must be emphasized that this value is very well constrained by the model inasmuch as the adjustments to the observed trends are sensitive to a small fluctuation of X^{opx}. This X^{opx} value is valid for the first most magnesian linear trend up to the inflection in TiO_2 and V concentrations that takes place around $F = 0{\cdot}7$. This inflection implies an increase in the bulk partition coefficient consistent with the appearance of Fe–Ti oxide minerals on the liquidus (hemo-ilmenite, ilmenite and/or Ti-magnetite). For F values below 0·7, the second TiO_2 vs MgO linear trend cannot be modelled quantitatively because we ignore the nature of the Fe–Ti oxide minerals, their proportion and their partition coefficients. It is noteworthy that the change in slope is not observed for the other elements. A simple calculation shows that when the added mineral has a $D_i^{j/\mathrm{liq}}$ value close to the D_i^{bulk}, the contribution of this mineral to the D_i^{bulk} is balanced by a decrease in the contribution of the other minerals. This is in all likehood the case for MgO, MnO, Ni and Co. For Zn, its incompatible behaviour is not modified by the appearance of the Fe–Ti oxide mineral.

The Rayleigh model, however, fails to explain the Cr evolution. The overall decrease of Cr with fractional crystallization in the centre grossly reflects its compatible character in orthopyroxene and the decrease that follows in the melt. A more quantitative approach is, however, not permitted because the $D_{\mathrm{Cr}}^{\mathrm{opx}}$ does not remain constant during polybaric evolution. It has been shown experimentally that $D_{\mathrm{Cr}}^{\mathrm{opx}}$ strongly varies with pressure from

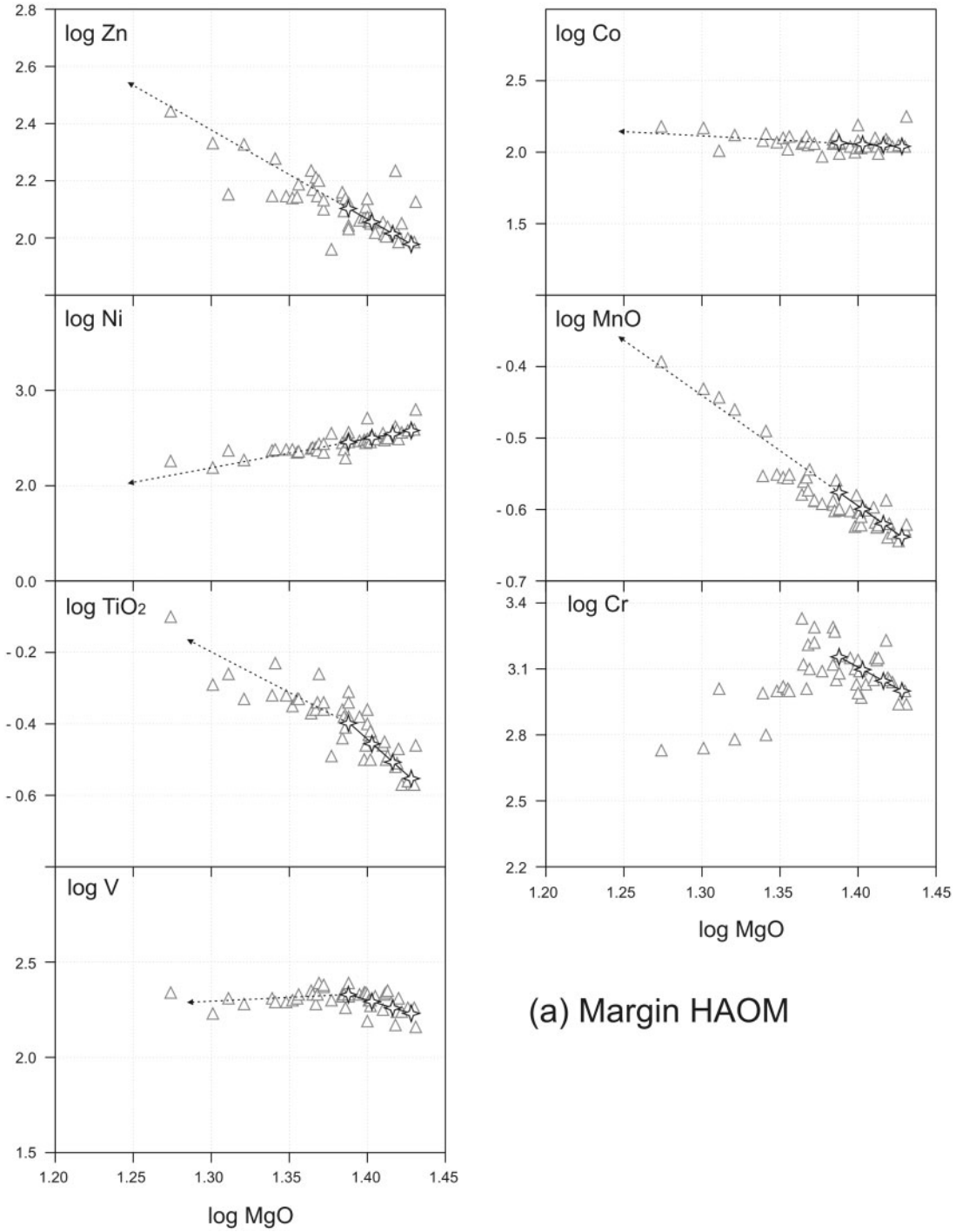

Fig. 13. Rayleigh fractional crystallization modelling of HAOM compositions from (a) the margin and (b) the centre of EGOG. The linear trends represent the evolution of the pyroxene calculated by the model, the stars mark the values at $F = 1$, 0·9, 0·8, and 0·7. Beyond $F = 0{\cdot}7$, the model is only qualitatively estimated. F, fraction of liquid remaining.

$D_{Cr}^{opx} = 2$ at 1 atm to 14 at 10 kbar (Vander Auwera *et al.*, 2000). Disordered variations of Cr contents at high MgO values in the centre HAOM might also be related to zoning of the crystals as suggested by variations in samples taken from the same outcrop. The increase of Cr with decreasing MgO in the margin HAOM is enigmatic, because explaining it by fractional crystallization would require an unexpectedly low D_{Cr}^{opx} value.

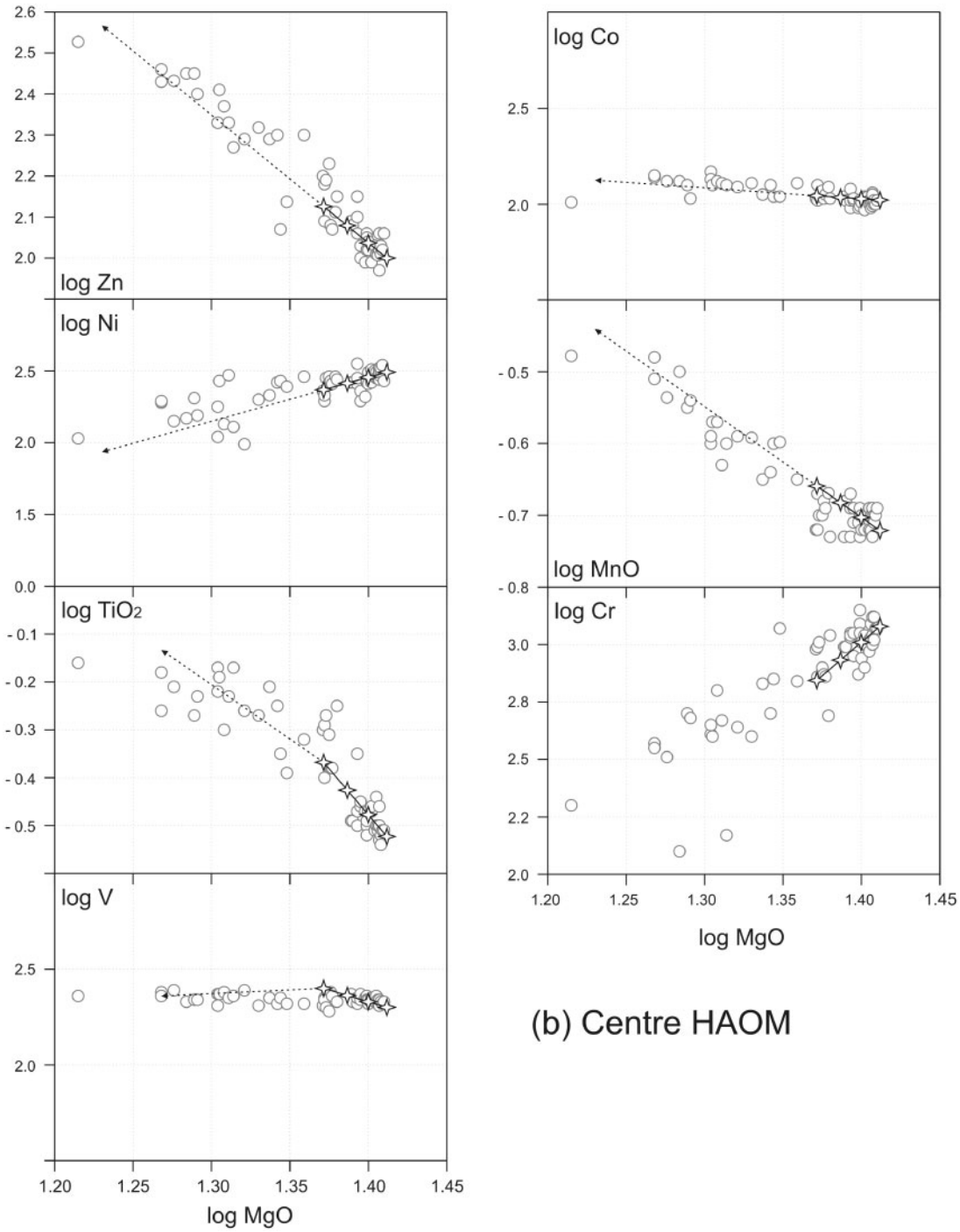

Fig. 13. Continued.

The D_i^{opx} values for Zn, Ni, Co, V, Mn and Ti that result from the modelling are reported in Table 4 together with the average concentrations of the five most Mg-rich HAOM from the margin and centre of the EGOG anorthosite. Inversion to the melt compositions was carried out in an attempt to further constrain the parental magma compositions and to compare them with some chilled rocks; for example, sample SG, a fine-grained dyke of high-alumina basalt composition, and sample TJ, a primitive jotunite (Table 3). The agreement is very good for Co, Ni and Mn, for which the inverted values are within error of the chill contents. TiO_2 is also in good

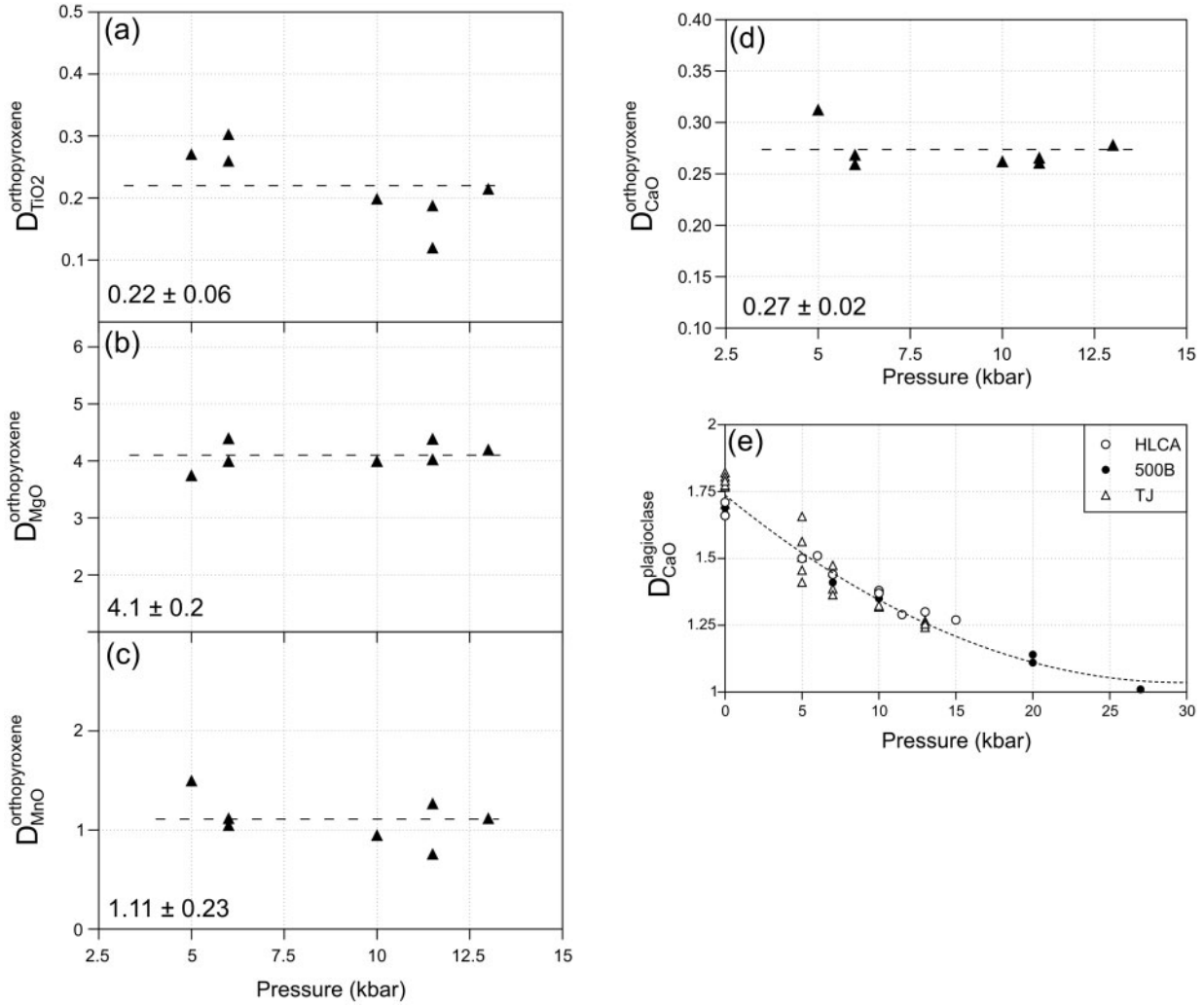

Fig. 14. (a–d) Partition coefficients for TiO_2, MgO, MnO and CaO between orthopyroxene and melt obtained at various pressures (from 5 to 13 kbar) and close to the liquidus temperatures from the experimental data of Fram & Longhi (1992) and Longhi *et al.* (1999) on HLCA. (e) Partition coefficient for CaO between plagioclase and melt as a function of pressure from the experimental studies of Fram & Longhi (1992), Vander Auwera & Longhi (1994) and Longhi *et al.* (1999) on several different melt compositions.

agreement with HLCA and SG. V values are lower than in TJ and SG, but this may result from oxygen fugacity differences between the parental melts and the chills (Toplis & Corgne, 2002). Inverted Zn values, which are higher than in TJ and SG, are affected by a large error. We used $D^{opx}_{Cr} = 14$, a value obtained at 11 kbar (Vander Auwera *et al.*, 2000), and obtained inverted values close to the content in the high-alumina gabbro SG. This further corroborates the hypothesis that high-alumina basaltic melts are the parental magmas of both the centre and margin of the EGOG.

The fractional crystallization modelling of the HAOM permits the following conclusions:

(1) variation in pressure controls the Al content of HAOM, but has no influence on the Mg-number of the HAOM;
(2) cotectic assemblages include only plagioclase and orthopyroxene, the proportions of which are constant at the beginning of the evolution ($F = 1$–$0{\cdot}7$) in both melts ($X^{opx} = 0{\cdot}33$);
(3) Fe–Ti oxide minerals join the liquidus assemblage at $F \sim 0{\cdot}7$ in both magmas;
(4) the appearance of Fe–Ti oxide minerals on the liquidus, the Al content of the HAOM and the variations in P–T conditions have no detectable influence on the behaviours of Zn, Ni, Co and Mn;
(5) owing to variation of D^{opx}_{Cr} with pressure and possibly to zoning of the HAOM, the model does not adequately explain the Cr behaviour;
(6) high-alumina basaltic melts similar to HLCA and SG are possible parental melts to both the central and marginal anorthosites, but the centre parental melt is

Table 4: Partition coefficients between orthopyroxene and melt obtained by modelling, composition of the less evolved HAOM (average of five samples) in the centre and margin of the EGOG massif, inverted values in centre and margin melts, and observed values in possible parental magmas

	D calculated	Content in centre HAOM	Content in margin HAOM	Content in centre melt	Content in margin melt	TJ (Tjörn jotunite)	SG (Saglands-vatn)	HLCA (Harp Lake)
TiO_2	0·22 (10)	0·32 (2)%	0·31 (3)%	1·45 (67)%	1·41 (65)%	3·63%	1·30%	1·85%
MnO	1·3 (1)	0·20 (1)%	0·24 (1)%	0·15 (1)%	0·18 (1)%	0·15%	0·18%	0·15%
Co	2·2 (2)	104 (6)	120 (22)	47 (5)	55 (11)	49	52	n.a.
Ni	5·7 (3)	314 (22)	380 (96)	55 (5)	67 (17)	60	71	n.a.
V	1·15 (20)	215 (6)	187 (28)	187 (33)	163 (37)	216	249	n.a.
Zn	0·20 (2)	105 (6)	113 (23)	525 (59)	565 (74)	144	99	n.a.
Cr	14 (1)*	1110 (125)	1200 (260)	79 (9)	86 (19)	28	74	n.a.

*From Vander Auwera *et al.* (2000).
Values in ppm except when indicated; values in parentheses represent the standard deviation (1σ); n.a., not available.

lower in Cr and MnO and also in CaO as deduced from the composition of the plagioclase megacrysts (see below).

Modelling the plagioclase composition

Fractional crystallization modelling can also be applied to plagioclase and, particularly, to the plagioclase megacrysts that are associated in sub-ophitic texture with the HAOM. The Rayleigh equation when written for plagioclase implies knowledge of X^{plag}, D^{plag}_{CaO}, D^{opx}_{CaO}, D^{plag}_{Sr}, D^{plag}_{K}, D^{plag}_{Ba}, D^{plag}_{Ti} and D^{plag}_{Fe}, whose values can be defined in the following way.

(1) As plagioclase is the only mineral to coexist with HAOM for a melt fraction evolving from unity to 0·7, it directly results from the HAOM modelling that $X^{plag} = 1 - X^{opx} = 0{\cdot}67$.

(2) The D^{opx}_{CaO} value is determined with the same experimental dataset as used to determine D^{opx}_{MgO}. The value of D^{opx}_{CaO} is $0{\cdot}27 \pm 0{\cdot}02$, which is invariant with pressure (Fig. 14).

(3) In the same way as for modelling of the HAOM, the D^{plag}_{CaO} values can be estimated from the experimental data of Longhi and co-workers at pressures ranging from 1 atm to 20 kbar on three melt compositions: HLCA (the Harp Lake high-alumina basalt), TJ (Tjörn jotunite) and 500B (an anorthositic dyke composition) (Fram & Longhi, 1992; Vander Auwera & Longhi, 1994; Longhi *et al.*, 1999; Vander Auwera *et al.*, 2000). D^{plag}_{CaO} is defined by the ratio of the CaO content in plagioclase to the CaO content in the coexisting melt at or near-liquidus temperatures. The values are plotted as D^{plag}_{CaO} vs pressure in Fig. 14. It appears that there are insignificant differences between the three magma types; thus a unique regression can be performed with a good fit ($r = 0{\cdot}97$) to the data:

$$D^{plag}_{CaO} = 0{\cdot}001P^2(\text{kbar}) - 0{\cdot}047P(\text{kbar}) + 1{\cdot}737. \quad (1)$$

Provided the magma composition is known, D^{plag}_{CaO} can be also calculated at various pressures and temperatures following the model of Putirka (2005). Values calculated at the liquidus temperature of 1275°C for high-alumina basalts (Fram & Longhi, 1992) and of 1187°C for primitive jotunite (Vander Auwera & Longhi, 1994) are reported in Table 3. Although there is a noticeable effect of melt composition, the values of D^{plag}_{CaO} on average are close to that calculated with equation (1) (see below, Table 5), and the similarity to the value for SG is probably not coincidental.

(4) The An content of plagioclase depends on pressure and on the CaO content of the conjugate melt. As already pointed out, two different melts are proposed to account for the two groups of high-pressure plagioclase in the central anorthosite. We propose for the first magma 'pulse' the CaO concentration of Tjörn (TJ) (6·8 wt %), and for the second magma 'pulse', a higher CaO concentration of 8·0 wt %. At a defined pressure, D^{plag}_{CaO} can be calculated with equation (1) and the An content of plagioclase follows (Table 5).

(5) For the partition coefficients of K and Ba, we have adopted the semi-empirical relationships of Bindeman *et al.* (1998), which are in the form $RT \ln D = aX_{An} + b$. At a given pressure, the CaO content of plagioclase may be calculated from the CaO content in the liquid and equation (1), and

Table 5: Partition coefficients between plagioclase and melt used in modelling the EGOG plagioclase composition

	Margin HLCA				Centre 1st pulse					Centre 2nd pulse	
P (kbar):	10	7	5	3	13	10	7	5	3	11·5	7
T (°C):	1275	1250	1200	1150	1187	1175	1170	1167	1162	1235	1215
An %:	59·5	63·5	66·5	69·9	43·8	46·3	49·3	51·7	54·3	53·0	58·0
K[1]	0·14	0·12	0·11	0·09	0·17	0·16	0·15	0·14	0·13	0·15	0·13
Ba[1]	0·35	0·29	0·24	0·19	0·66	0·59	0·51	0·46	0·41	0·45	0·36
Fe[2]	0·04	0·04	0·04	0·04	0·04	0·04	0·04	0·04	0·04	0·04	0·04
Ti[3]	0·041	0·036	0·030	0·024	0·049	0·045	0·042	0·039	0·036	0·044	0·037
Sr[4]	1·37	1·49	1·58	1·67	1·67	1·88	2·09	2·23	2·36	1·47	1·70
Ca[5]	1·37	1·46	1·53	1·61	1·30	1·37	1·46	1·53	1·61	1·33	1·46

[1]From Bindeman *et al*. (1998).
[2]Value invariant with *T*, between 0·043 ± 0·005 (Aigner-Torres *et al.*, 2007) and our measured value of 0·037 ± 0·009.
[3]Fitted to the values of $D_{Ti} = 0{\cdot}042$ for An_{58} and 1270°C.
[4]From Vander Auwera *et al*. (2000).
[5]From equation (1) (this work).

An (wt %) = 4·961 × CaO(plag). An estimate of the temperature is given by the experimentally determined pressure–temperature phase diagrams for HLCA (Fram & Longhi, 1992) and TJ (Tjörn) (Vander Auwera & Longhi, 1994). For D_{Fe}^{plag}, the value calculated with the approach of Bindeman *et al*. (1998) for the margin plagioclase (i.e. $D_{Fe}^{plag} = 0 \cdot 084$) is much higher than that obtained (0·037 ± 0·009) by ratioing the average Fe concentration of plagioclase and the concentration in HLCA. A value of 0·040, close to the value of 0·046 found by Aigner-Torres *et al*. (2007) for fO_2 conditions below the fayalite–magnetite–quartz buffer (FMQ) is adopted here for the margin and the centre compositions and, as no temperature dependence has been demonstrated by these workers, it is considered constant. For Ti, we have calculated D_{Ti}^{plag} as the ratio of the Ti concentrations in An_{58} plagioclase and HLCA and obtained 0·042 ± 0·005, a value similar to that found for basaltic compositions by Aigner-Torres *et al*. (2007). To account for the temperature dependence, we have fitted the Bindeman *et al*. (1998) relationship to our value for An_{58} and 1270°C. The values obtained are reported in Table 5.

(6) Several recent studies have focused on the determination of D_{Sr}^{plag} [see the discussion by Vander Auwera *et al*. (2000)] and point to a strong inverse correlation between D_{Sr}^{plag} and the anorthite content of plagioclase. Plagioclase becomes more albitic with increasing pressure, so an increase in pressure would also indirectly increase D_{Sr}^{plag}. Vander Auwera *et al*. (2000) have experimentally shown, however, that, on the contrary, D_{Sr}^{plag} decreases slightly with pressure. These workers have further suggested that the behaviour of D_{Sr}^{plag} results from the combined effects of increasing temperature and pressure counterbalancing the effects of plagioclase crystal chemistry. Because the ionic radius of Sr^{2+} is significantly higher than those of Ca^{2+} and Na^{+}, a pressure increase would not favour the solubility of Sr in plagioclase. We adopt here the expression correcting the Blundy & Wood (1991) (BW) values for the influence of pressure proposed by Vander Auwera *et al*. (2000): $\ln D_{Sr}^{plag} = \ln D_{Sr}^{plag}$ (BW) $- 0{\cdot}082P$ (bar)/T (K) (Table 5).

These parametric values introduced in the Rayleigh equation lead to the models graphically represented in Figs 15 and 16. Figure 15 deals with the low-Sr plagioclase from the margin and shows the result of the fractional crystallization modelling at 5, 7 and 10 kbar. Figure 16 concerns the high-Sr plagioclase from the centre and shows the evolution of the various elements in a pressure range from 13 kbar to 3 kbar, starting from a plagioclase of An_{45} that crystallizes in the first pulse of magma (6·8% CaO). Figure 16f is related to the evolution at 11·5 and 7 kbar of plagioclase starting at An_{53} and crystallizing in the second 'pulse' of melt (8·0% CaO). At each pressure, D_{CaO}^{plag} is calculated with equation (1), and knowing the CaO content of the melt, we obtain the starting composition of the plagioclase, CaO_0. The Sr concentration of plagioclase, Sr_0, is taken in the observed range of values (920–950 ppm in the centre and 430–450 ppm in the margin). There is a very limited range of concentrations that can be explained by fractional crystallization at a given pressure. This is essentially due to the fact that the values of D_{CaO}^{plag} and D_{Sr}^{plag} are close to the 1·5–2·0 range,

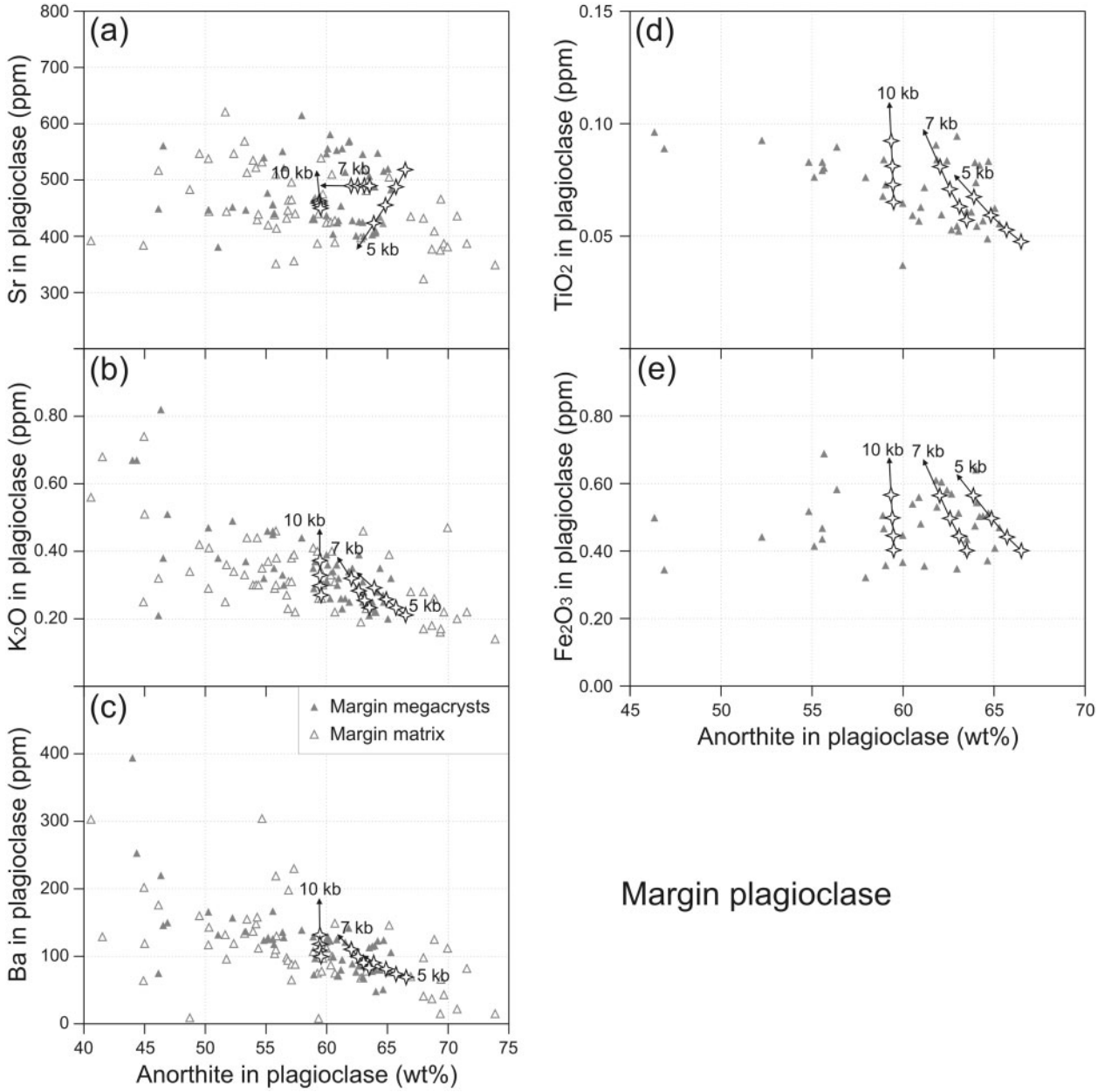

Fig. 15. Modelling of the margin plagioclase composition at pressures of 5, 7 and 10 kbar during fractional crystallization. The lines represent the evolution of the plagioclase compositions and the stars the values at F values from 1·0 to 0·7.

which yields bulk partition coefficients close to unity for the cotectic assemblage in both magmas. To account for the entire range of compositions, it is necessary to crystallize the magmas at different pressures.

The model represented in Fig. 16a–e in which the melt has the CaO content of TJ (6·8 wt %) exhibits unusual behaviour at 13 kbar: the An content in plagioclase increases with decreasing temperature (see below). Moreover, a second group of plagioclase averaging An_{53} associated with HAOM whose barometry predicts crystallization between 10 and 12 kbar (Fig. 10) is predicted by the Rayleigh model to have crystallized between 3 and 5 kbar. To explain the An_{53} plagioclase at high pressure, we are forced to posit a second magma 'pulse' with a higher CaO content. We show in Fig. 16f the modelling at 11·5 kbar and 7 kbar of the Sr–An relationship of plagioclase crystallizing from this second melt with a CaO content of 8 wt %. The second magma accounts for the group of plagioclase compositions at An_{53}, but leaves plagioclase with lower An contents unexplained.

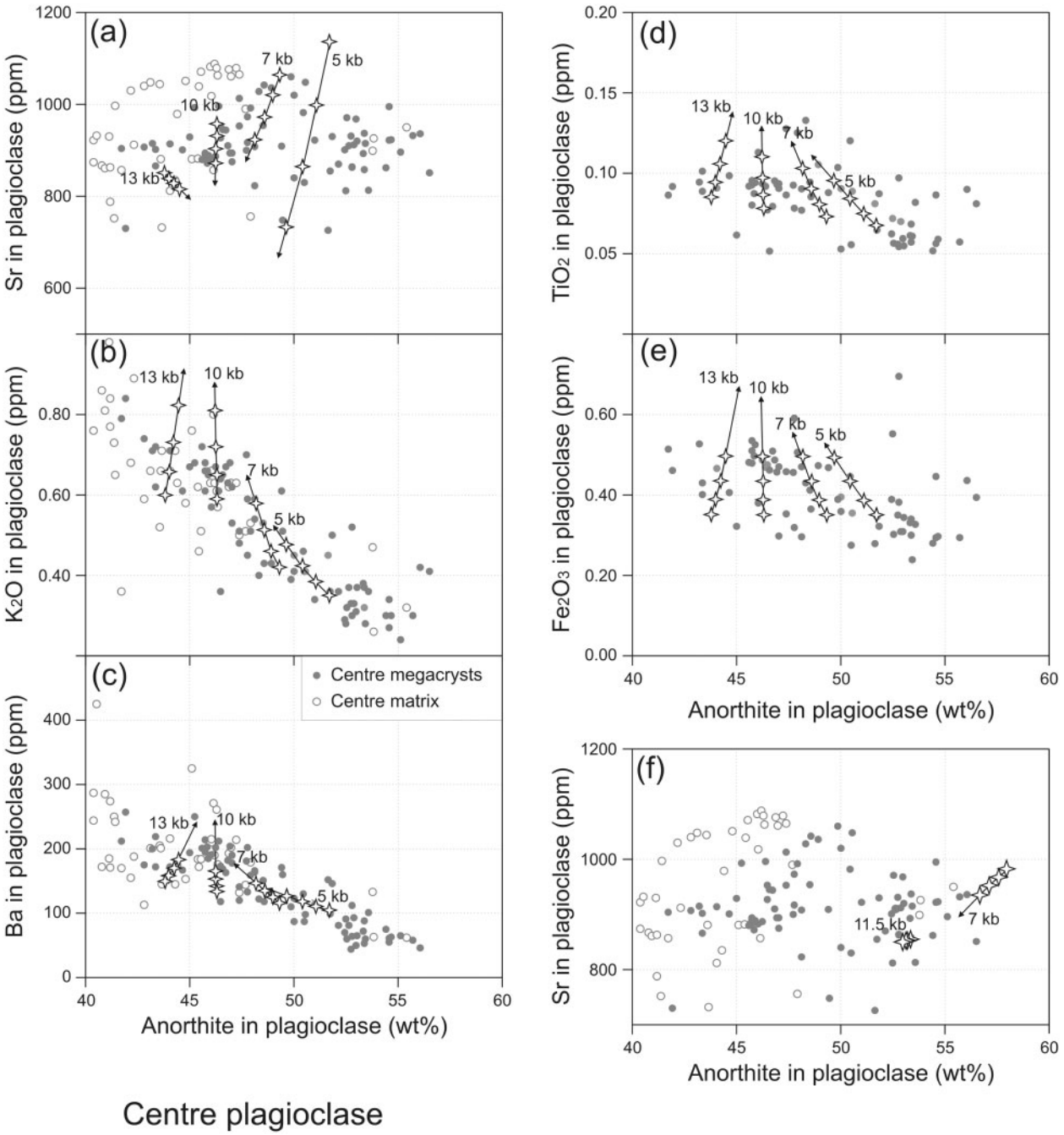

Fig. 16. (a–e) Modelling of the centre plagioclase at pressures of 5, 7, 10 and 13 kbar during fractional crystallization from $F = 1{\cdot}0$ to $0{\cdot}7$ using a melt with CaO = 6·82 wt % (first 'pulse' of melt in the central anorthosite). (f) Modelling of the centre plagioclase at pressures of 7 and 11·5 kbar during fractional crystallization from $F = 1{\cdot}0$ to $0{\cdot}7$ using a melt with CaO = 8·02 wt % (second 'pulse' of melt in the central anorthosite). Lines and stars as in Fig. 15.

The same modelling was applied to Ba, K, Fe and Ti in plagioclase from the centre and the margin (Figs 15 and 16). The same conclusions as derived from the Sr modelling can be drawn: the overall trends can be explained by fractionation at a series of pressures from 3 to 13 kbar with production of plagioclase with a limited compositional range at each pressure. The calculated lines of descent can be almost parallel to the overall trend (e.g. Ba vs An at 3 and 5 kbar in the centre), which points to crystallization as the major factor in producing the dispersion of

compositions. Alternatively, modelling can yield nearly vertical trends (e.g. K vs An in the margin, Fe and Ti vs An in the margin), which points to pressure as being the major factor in producing the dispersion of compositions for those elements.

The centre and margin magmas thus crystallized continuously along a P–T gradient starting at 10–13 kbar and ending at 4–5 kbar. The margin magma mainly crystallized in the 6–8 kbar range, whereas the central magmas have done so between 9 and 12 kbar. During diapiric ascent, decreasing pressure is the main control on plagioclase compositions and the Al content of HAOM, and decreasing temperature controls the Mg-number of HAOM. It also follows that the centre of the EGOG anorthosite was formed by at least two magma 'pulses', with different CaO contents but similar Mg-numbers.

On the increase of the An content with decreasing temperature

The properties of the albite–anorthite system at high pressure have been addressed by Lindsley (1969). He showed experimentally that with increasing pressure an azeotrope with a maximum develops in the plagioclase loop. The temperature maximum migrates towards higher Ab contents with increasing pressure. The exchange coefficient $K_{\mathrm{Dplag-liq}}^{\mathrm{An-Ab}}=(X_{\mathrm{Ab}}^{\mathrm{plag}}\cdot X_{\mathrm{An}}^{\mathrm{liq}})/(X_{\mathrm{Ab}}^{\mathrm{liq}}\cdot X_{\mathrm{An}}^{\mathrm{plag}})$, with X_{An} and X_{Ab} being the mole fractions of anorthite and albite respectively, is 1·0 only at the maximum of the azeotrope. On the sodic side of the azeotrope K_{D} is <1 and plagioclase–liquid partitioning is normal. On the calcic side of the maximum K_{D} is >1 and plagioclase–liquid partitioning is reversed. On the basis of experiments at various pressures, including those of Fram & Longhi (1992), Morse (2006, 2008) showed that $K_{\mathrm{D}}=1$ at *c.* 15 kbar. Our analysis of the experiments in Fig. 14e also shows that $D_{\mathrm{CaO}}^{\mathrm{plag}}$ approaches 1·0 at pressures above 20 kbar. In our model the increase in the An content of plagioclase with fractional crystallization in cotectic proportions with orthopyroxene at 13 kbar (Fig. 16a) confirms the existence of the plagioclase azeotrope.

The role of trapped liquid crystallization

The margin plagioclase compositions from the EGOG anorthosite extend towards andesine compositions (Fig. 17) that cannot be accounted for by the present model. Starting from the HLCA melt composition, andesine plagioclase would require pressure conditions higher than those considered here, which are unrealistic as they are outside the stability field of plagioclase + orthopyroxene (Fram & Longhi, 1992). However, we observe that the melts in equilibrium with plagioclase are slightly lower in Sr and Ca than the plagioclase (Fig. 17). It is thus plausible that the andesine plagioclase results, at least in part, from a reaction between a labradorite plagioclase and the interstitial melt of the crystal mush. The same remark holds also true for the centre plagioclase with An contents less than 43.

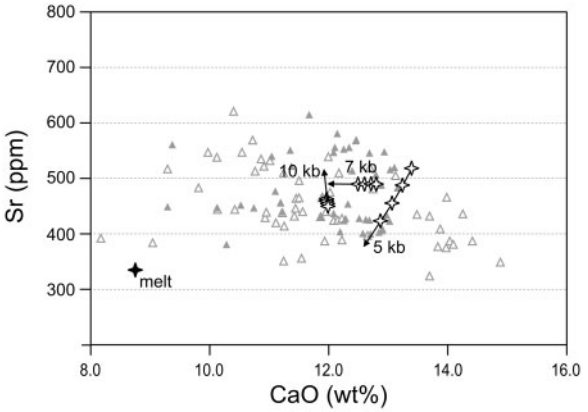

Fig. 17. Relationship between margin plagioclase and parental melt composition and fractional crystallization from $F=1{\cdot}0$ to 0·7. Symbols as in Fig. 15.

Composition of the parental magmas

Some characteristics of the parental magma compositions can be drawn from the modelling of the HAOM and plagioclase. A high-alumina basaltic composition similar to HLCA or SG is adequate for the margin. The two parental magmas of the central part are possibly high-alumina basalts with Mg-numbers similar to the margin magma but with distinctly lower Ca and higher Sr concentrations, which yield a Sr-rich andesine to labradorite plagioclase at high pressure, compared with a Sr-poor labradorite plagioclase in the margin magma. The centre magmas are also poorer in Cr and Mn than the margin magma. All the putative parent magmas have a normative wollastonite content lower than present-day basaltic magmas (Longhi *et al.*, 1999; Longhi, 2005).

We are aware that we have to account for the puzzling occurrence of three magmas with similar Mg-numbers but different CaO contents. How can different types of high-alumina basalts be produced at depth, almost simultaneously, with low wollastonite contents, grossly the same Mg-number, but different CaO contents? Longhi and co-workers (Longhi *et al.*, 1999; Longhi, 2005) have argued that such magmas can be produced only by partial melting of a gabbronoritic source at depths corresponding to pressures of 10–13 kbar. Clearly, more work is needed to constrain the nature of the source and the melting process.

Another important output of the present model concerns the nature of the parental magmas of the Rogaland anorthosite. The occurrence of jotunitic chilled margins to the Hidra body (Demaiffe & Hertogen, 1981) and the Bjerkreim–Sokndal layered intrusion (Duchesne & Hertogen, 1988; Robins *et al.*, 1997) led to the proposition

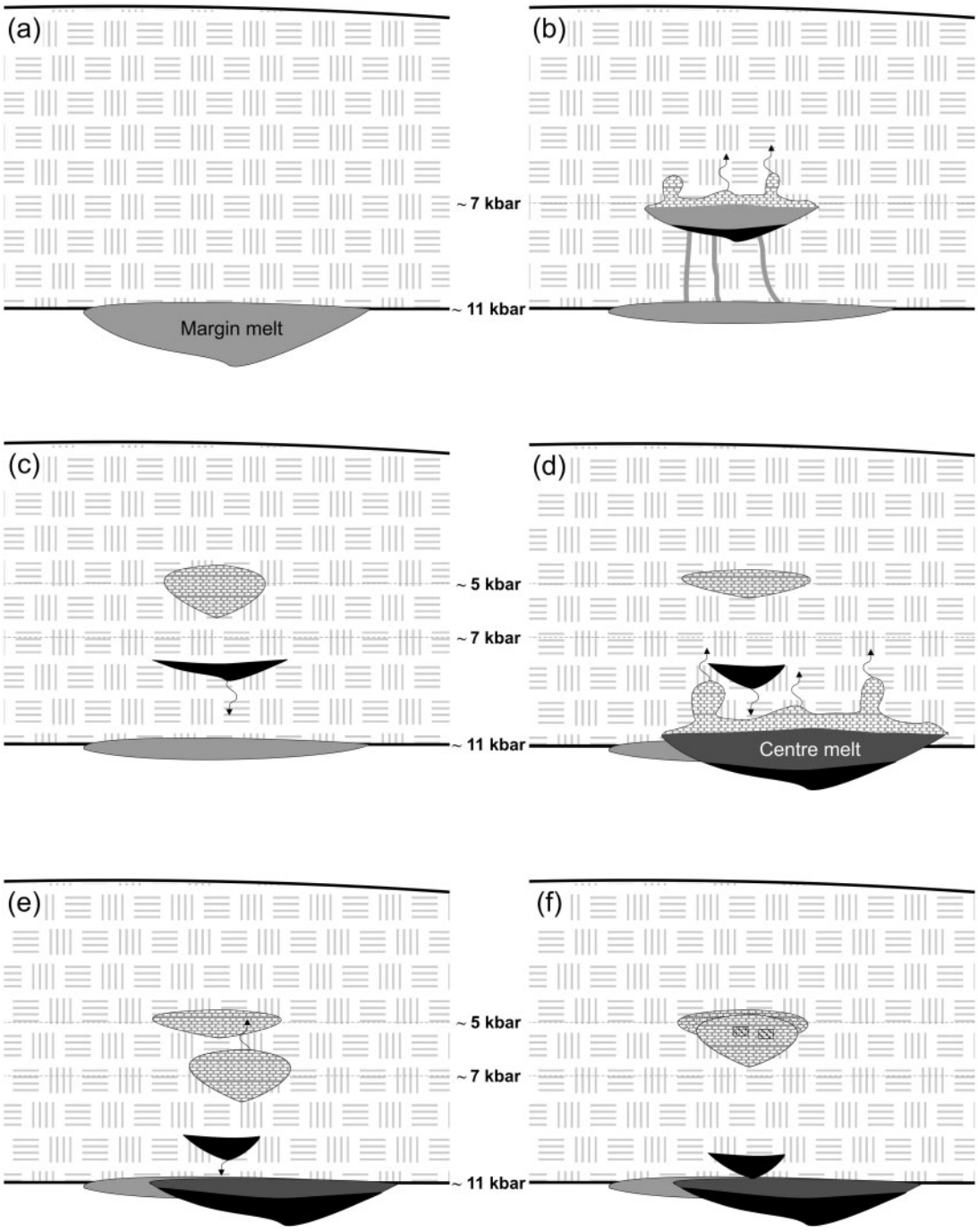

Fig. 18. Synthetic model for the emplacement of the Egersund–Ogna massif-type anorthosite. (a) Ponding at the base of the crust of the parental high-alumina basalt, which started crystallizing at *c.* 10–11 kbar. (b) Ascent of the magma to a second chamber at *c.* 7 kbar, where it crystallized most of the HAOM (5–7 wt % Al_2O_3) and labradorite plagioclase. Accumulation of a plagioclase crystal mush at the roof of the chamber. (c) This anorthositic mush rose diapirically with polybaric crystallization of plagioclase and HAOM en route to the final level of emplacement (*c.* 5 kbar). (d) Formation of new high-alumina basaltic melts at depth and crystallization of andesine to labradorite roof cumulate with high-Al HAOM (7–9 wt % Al_2O_3). (e) Crystallization of HAOM with decreasing Al contents and plagioclase with increasing anorthite contents en route to the final emplacement pressure. (f) Rise of the composite andesine anorthosite diapir that intruded and deformed the marginal labradorite anorthosite.

of jotunite as a possible parental melt to andesine anorthosites. However, the high Cr contents of the HAOM found in the EGOG anorthosite compared with low Cr contents in orthopyroxene from the Hidra body or the Bjerkreim–Sokndal intrusion have pointed to another composition, more basaltic and richer in Cr, for the EGOG massif (Duchesne & Demaiffe, 1978; Duchesne *et al.*, 1985; Duchesne & Maquil, 1987). On the basis of experimental data on the stability of HAOM and plagioclase (Longhi *et al.*, 1999) and on the D_{Cr}^{opx} (Vander Auwera *et al.* 2000), the EGOG central anorthosite was subsequently considered to have crystallized from a jotunitic magma, slightly more magnesian than TJ (Tjörn, see discussion above), whereas the EGOG margin formed from a high-alumina basalt. The present study, however, suggests that the centre of the EGOG is also produced from a high-alumina basaltic melt. Longhi (2005) indicated that fractional crystallization is not a suitable mechanism to explain the variation within the group of anorthosite parent magmas.

Emplacement scenario

The model of Emslie (1980) must be slightly revised to account for a continuum in the P–T evolution of the HAOM and the presence in the same intrusion of anorthosite that crystallized from at least two different magmas (Fig. 18). The transition between the centre and margin samples, despite subcontinuous outcrops in the field, is nowhere marked by any intrusive contacts. The occurrence of blocky inclusions from the deformed margin, as shown by the Sr–Ca contents of plagioclase (Fig. 11), however, indicates that the margin rocks were formed prior to the centre. The first magma to be generated was thus a high-alumina basalt (such as HLCA), which started crystallizing plagioclase and HAOM with a high alumina content at a pressure of *c.* 10 kbar. The magma then ascended to a second chamber at intermediate crustal depth, between 21 and 28 km (6–8 kbar), where it crystallized most of the HAOM (now with 5–7 wt % Al_2O_3) together with labradorite plagioclase, and a plagioclase crystal mush accumulated by flotation at the roof of the chamber. As a result of gravity instabilities, the anorthositic mush rose diapirically, and plagioclase and HAOM continued to crystallize in batches of residual liquid at each pressure en route to the final level of emplacement (*c.* 18 km; 5 kbar). At that stage, a second and third high-alumina basaltic melt were formed at depth and their crystallization yielded a heterogeneous andesine to labradorite roof cumulate with HAOM (7–9 wt % Al_2O_3), which in turn was able to form a batch of rising anorthosite. Again, HAOM with decreasing Al contents and plagioclase with increasing anorthite contents crystallized en route to the final emplacement pressure. The composite diapir eventually intruded the margin labradorite anorthosite, which was not completely solidified, and deformed it together with the gneiss envelope by ballooning. The tail of the andesine anorthosite diapir was progressively telescoped into the central part of the intrusion.

The emplacement and crystallization of the EGOG anorthosites was followed by the intrusion of noritic dykes, mostly pegmatitic, containing HAOM of intermediate Al content (Maquil & Duchesne, 1984), and by a system of jotunitic dykes of various compositions, indicating that magmatic processes remained active for some time. The emplacement scenario still needs a deep-seated magma chamber as proposed by Emslie (1980, 1991), but we now conceive the diapir as made up of a collection or mosaic of domains that have crystallized separately at each pressure en route to the final depth of emplacement.

The mechanism of formation of the EGOG intrusion can explain the common occurrence of andesine and labradorite anorthosite either in the same intrusion or as inclusions of the latter within the former, as described, for example, by Anderson & Morin (1969), Dymek (2004) and Owens & Dymek (2005).

CONCLUSIONS

Plagioclase from the centre of the Egersund–Ogna anorthosite in the Rogaland anorthosite province of SW Norway is mostly andesine with some labradorite, whereas in the margin labradorite dominates with some andesine. The Sr concentration of plagioclase is distinctly higher in the centre than in the margin.

The HAOM from the centre and margin show similar ranges of Mg-number and trace element contents; they differ only in their Mn and Cr contents, which are higher in the margin. The Al contents of the HAOM record continuous variations in the pressure of formation from 12 kbar down to 5 kbar in the centre, with maximum values at 10 kbar, whereas in the margin the range covers an interval of 3–10 kbar with maximum values between 6 and 8 kbar. The trace element evolution of the HAOM can be modelled by a fractional crystallization process, independent of pressure, starting with a leuconoritic cotectic assemblage (0·33 orthopyroxene + 0·67 plagioclase). Fe–Ti oxide minerals probably join the liquidus phases after about 30% crystallization. The plagioclase compositions depend strongly on pressure and less on extent of fractional crystallization and temperature.

The parent magma of the margin was most probably a wollastonite-poor high-alumina basalt similar to marginal rocks from the Harp Lake complex, Labrador. In the centre, two distinct high-alumina basaltic magmas are needed to explain the range of An values in plagioclase. They differ in their CaO contents, which are lower than in HLCA. Both are richer in Sr than the margin magma, but have the same Mg-number as the latter. Crystallization along a P–T gradient of HAOM and plagioclase

takes place partly in magma chambers but also en route in the rising diapir.

ACKNOWLEDGEMENTS

We acknowledge the help in the field or in the data processing of H. Diot, O. Bolle, J.-M. Lambert, Th. Lambé, L. Oury and P. Ntirabamba. We are grateful to Guy Bologne for his continuous help in the chemical analyses. The thorough reviews of J. S. Scoates and J. H. Bédard greatly improved the science and presentation of the paper.

FUNDING

The Belgian FNRS is thanked for financial assistance. This is Lamont-Doherty Earth Observatory Contribution No. 7413.

SUPPLEMENTARY DATA

Supplementary data for this paper are available at *Journal of Petrology* online.

REFERENCES

Aigner-Torres, M., Blundy, J., Ulmer, P. & Pettke, T. (2007). Laser ablation ICPMS study of trace element partitioning between plagioclase and basaltic melts: an experimental approach. *Contributions to Mineralogy and Petrology* **153**, 647–667.

Anderson, A. T. & Morin, M. (1969). Two types of massif anorthosite and their implications regarding the thermal history of the crust. In: Isachsen, Y. W. (ed.) *Origin of Anorthosite and Related Rocks. New York State Museum and Science Service Memoir* **18**, 57–69.

Ashwal, L. D. (1993). *Anorthosites*. Heidelberg: Springer, 422 p.

Barnichon, J.-D., Havenith, H., Hoffer, B., Charlier, R., Jongmans, D. & Duchesne, J. C. (1999). The deformation of the Egersund Ogna massif, South Norway: Finite element modelling of diapirism. *Tectonophysics* **303**, 109–130.

Bédard, J. H. (2001). Parental magmas of the Nain plutonic suite anorthosites and mafic cumulates: a trace element modelling approach. *Contributions to Mineralogy and Petrology* **141**, 747–771.

Berg, J. H. (1977). Dry granulite mineral assemblages in the contact aureoles of the Nain complex, Labrador. *Contributions to Mineralogy and Petrology* **64**, 33–52.

Bindeman, I. N., Davis, A. M. & Drake, M. J. (1998). Ion microprobe study of plagioclase–basalt partition experiments at natural concentration levels of trace elements. *Geochimica et Cosmochimica Acta* **62**, 1175–1193.

Bingen, B., Demaiffe, D. & van Breemen, O. (1998). The 616-My-old Egersund basaltic dike swarm, SW Norway, and the late Proterozoic opening of the Iapetus Ocean. *Journal of Geology* **106**, 565–574.

Blundy, J. D. & Wood, B. J. (1991). Crystal-chemical controls on the partitioning of Sr and Ba between plagioclase feldspar, silicate melts, and hydrothermal solutions. *Geochimica et Cosmochimica Acta* **55**, 193–209.

Bogdanova, S. V., Pashkevich, I. K., Buryanov, V. B., Makarenko, I. B., Orlyuk, M. I., Skobelev, V. M., Starostenko, V. I. & Legostaeva, O. V. (2004). The 1·80–1·74-Ga gabbro–anorthosite–rapakivi Korosten Pluton in the Ukrainian Shield: a 3-D geophysical reconstruction of deep structure. *Tectonophysics* **381**, 5–27.

Corrigan, D. & Hanmer, S. (1997). Anorthosites and related granitoids in the Grenville orogen: a product of convective thinning of the lithosphere? *Geology* **25**, 61–64.

Demaiffe, D. & Hertogen, J. (1981). Rare earth element geochemistry and strontium isotopic composition of a massif-type anorthositic–charnockitic body: the Hidra massif (Rogaland, SW Norway). *Geochimica et Cosmochimica Acta* **45**, 1545–1561.

Duchesne, J. C. & Demaiffe, D. (1978). Trace elements and anorthosite genesis. *Earth and Planetary Science Letters* **38**, 249–272.

Duchesne, J. C. & Hertogen, J. (1988). Le magma parental du lopolithe de Bjerkreim–Sokndal (Norvège méridionale). *Comptes Rendus de l'Académie des Sciences* **306**, 45–48.

Duchesne, J. C. & Korneliussen, A. (eds) (2003). *Ilmenite deposits and their geological environment, with special reference to the Rogaland Anorthosite Province, including a geological map at scale 1:75,000 and a CD with a guide to the province. Norges Geologiske Undersøkelse Special Publication* **9**, 138 p.

Duchesne, J. C. & Maquil, R. (1987). The Egersund–Ogna massif. In: Maijer, C. & Padget, P. (eds) *The Geology of Southernmost Norway: an excursion guide. Norges Geologiske Undersøkelse Special Publication* **1**, 50–56.

Duchesne, J. C., Roelandts, I., Demaiffe, D. & Weis, D. (1985*a*). Petrogenesis of monzonoritic dykes in the Egersund–Ogna anorthosite (Rogaland, S.W. Norway): trace elements and isotopic (Sr, Pb) constraints. *Contributions to Mineralogy and Petrology* **90**, 214–225.

Duchesne, J. C., Maquil, R. & Demaiffe, D. (1985*b*). The Rogaland anorthosites: facts and speculations. In: Tobi, A. C. & Touret, J. L. R. (eds) *The Deep Proterozoic Crust in the North Atlantic Province*. Dordrecht: Reidel, pp. 449–476.

Duchesne, J. C., Liégeois, J. P., Vander Auwera, J. & Longhi, J. (1999). The crustal tongue melting model and the origin of massive anorthosites. *Terra Nova* **11**, 100–105.

Dymek, R. F. (2004). Anorthosite magma revisited: field and petrographic evidence from the CRUML belt, Grenville Province, Quebec. *EOS Transactions of the American Geophysical Union* **85(17)**, *Joint Assembly Supplement JA513*, Abstract V51E-01.

Dymek, R. F. & Gromet, L. P. (1984). Nature and origin of orthopyroxene megacrysts from the St-Urbain anorthositic massif, Quebec. *Canadian Mineralogist* **22**, 297–326.

Emslie, R. F. (1975). Pyroxene megacrysts from anorthositic rocks: a new clue to the sources and evolution of the parent magmas. *Canadian Mineralogist* **13**, 138–145.

Emslie, R. F. (1980). Geology and petrology of the Harp Lake Complex, central Labrador: an example of Elsonian magmatism. *Geological Survey of Canada Bulletin* **293**, 1–136.

Emslie, R. F. (1985). Proterozoic anorthosite massifs. In: Tobi, A. C. & Touret, J. L. R. (eds) *The Deep Proterozoic Crust in the North Atlantic Provinces*. Dordrecht: Reidel, pp. 39–60.

Emslie, R. F. (1991). Granitoids of rapakivi granite–anorthosite and related associations. *Precambrian Research* **51**, 173–192.

Emslie, R. F., Hamilton, M. A. & Theriault, R. J. (1994). Petrogenesis of a Midproterozoic anorthosite–mangerite–charnockite–granite (AMCG) complex—isotopic and chemical evidence from the Nain Plutonic Suite. *Journal of Geology* **120**, 539–558.

Fram, M. & Longhi, J. (1992). Phase equilibria of dikes associated with Proterozoic anorthosite complexes. *American Mineralogist* **77**, 605–616.

Ghiorso, M. S. & Sack, R. O. (1995). Chemical mass transfer in magmatic processes IV. A revised and internally consistent

thermodynamic model for the interpolation and extrapolation of liquid–solid equilibria in magmatic systems at elevated temperatures and pressures. *Contributions to Mineralogy and Petrology* **119**, 197–212.

Jansen, J. B. H., Blok, R. J. P., Bos, A. & Scheelings, M. (1985). Geothermometry and geobarometry in Rogaland and preliminary results from the Bamble area. In: Tobi, A. C. & Touret, J. L. R. (eds) *The Deep Proterozoic Crust in the North Atlantic Provinces*. Dordrecht: Reidel, pp. 499–516.

Kushiro, I. & Fujii, T. (1977). Flotation of plagioclase in magma at high pressures and its bearing on the origin of anorthosite. *Proceedings of the Japan Academy, Series B* **53**, 262–266.

Lafrance, B., John, B. E. & Scoates, J. S. (1996). Syn-emplacement recrystallization and deformation microstructures in the Poe Mountain anorthosite, Wyoming. *Contributions to Mineralogy and Petrology* **122**, 431–440.

Lindsley, D. H. (1969). Melting relations of plagioclase at high pressures. In: Isachsen, Y. W. (ed.) *Origin of Anorthosite and Related Rocks. New York State Museum and Science Service Memoir* **18**, 39–46.

Longhi, J. (2005). A mantle or mafic crustal source for Proterozoic anorthosites? *Lithos* **83**, 183–198.

Longhi, J. & Ashwal, L. D. (1985). Two-stage models for lunar and terrestrial anorthosites: petrogenesis without a magma ocean. *Proceedings of the 15th Lunar and Planetary Science Conference, Part 2. Journal of Geophysical Research* **90(Supplement)**: C571–C584.

Longhi, J., Vander Auwera, J., Fram, M. & Monthieth, J. N. (1993). Pressure effects, kinetics and rheology of anorthositic and related magmas. *American Mineralogist* **78**, 1016–1030.

Longhi, J., Vander Auwera, J., Fram, M. S. & Duchesne, J. C. (1999). Some phase equilibrium constraints on the origin of Proterozoic (massif) anorthosites and related rocks. *Journal of Petrology* **40**, 339–362.

Maquil, R. & Duchesne, J. C. (1984). Géothermométrie par les pyroxènes et mise en place du massif anorthositique d'Egersund–Ogna (Rogaland, Norvège méridionale). *Annales de la Société Géologique de Belgique* **107**, 27–49.

Marker, M., Schiellerup, H., Meyer, G. B., Robins, B. & Bolle, O. (2003). Geological map of the Rogaland anorthosite province—scale 1:75000. In: Duchesne, J. C. & Korneliussen, A. (eds) *Ilmenite deposits and their geological environment. With special reference to the Rogaland Anorthosite Province. Norges Geologiske Undersøkelse Special Publication* **9**, Plate 1.

Martignole, J. & Schrijver, K. (1970). Tectonic significance and evolution of the Morin anorthosite, Grenville Province, Quebec. *Bulletin of the Geological Society of Finland* **42**, 165–209.

Michot, J. & Michot, P. (1969). The problem of anorthosites: the South Rogaland igneous complex, southern Norway. In: Isachsen, Y. W. (ed.) *Origin of Anorthosite and Related Rocks. New York State Museum Sciences Service Memoir* **18**, 399–410.

Mitchell, J. N., Scoates, J. S. & Frost, C. D. (1995). High-Al gabbros in the Laramie anorthosite complex, Wyoming—Implications for the composition of melts parental to Proterozoic anorthosite. *Contributions to Mineralogy and Petrology* **119**, 166–180.

Morse, S. A. (1975). Plagioclase lamellae in hypersthene, Tikkoatokhakh Bay, Labrador. *Earth and Planetary Science Letters* **26**, 331–336.

Morse, S. A. (2006). Labrador massif anorthosites: Chasing the liquids and their sources. *Lithos* **89**, 202–221.

Morse, S. A. (2008). The internal magma reservoir of large intrusions revealed by multiphase Rayleigh fractionation. *Journal of Petrology* **49**, 2081–2098.

Myers, J. S., Voordouw, R. J. & Tettelaar, T. A. (2008). Proterozoic anorthosite–granite Nain batholith: structure and intrusion processes in an active lithosphere-scale fault zone, northern Labrador. *Canadian Journal of Earth Sciences* **45**, 909–934.

Owens, B. E. & Dymek, R. F. (1995). Significance of pyroxene megacrysts for massif anorthosite petrogenesis: Constraints from the Labrieville, Quebec, pluton. *American Mineralogist* **80**, 144–161.

Owens, B. E. & Dymek, R. F. (2005). Rediscovery of the Mattawa anorthosite massif, Grenville Province, Quebec. *Canadian Journal of Earth Sciences* **42**, 1699–1718.

Putirka, K. A. (2005). Igneous thermometers and barometers based on plagioclase plus liquid equilibria: Tests of some existing models and new calibrations. *American Mineralogist* **90**, 336–346.

Robins, B., Tumyr, O., Tysseland, M. & Garman, L. D. (1997). The Bjerkreim–Sokndal layered intrusion, Rogaland, SW Norway: evidence from marginal rocks for a jotunite parent magma. *Lithos* **39**, 121–133.

Ryan, B. (2000). The Nain–Churchill boundary and the Nain Plutonic Suite: a regional perspective on the geologic setting of the Voisey's Bay Ni–Cu–Co deposit. *Economic Geology* **95**, 703–724.

Schärer, U., Wilmart, E. & Duchesne, J. C. (1996). The short duration and anorogenic character of anorthosite magmatism: U–Pb dating of the Rogaland complex, Norway. *Earth and Planetary Science Letters* **139**, 335–350.

Schiellerup, H., Korneliussen, A., Heldal, T., Marker, M., Bjerkgård, T. & Nilsson, L.-P. (2003). Mineral resources in the Rogaland Anorthosite Province, South Norway: origins, history and recent developments. In: Duchesne, J. C. & Korneliussen, A. (eds) *Ilmenite deposits and their geological environment. With special reference to the Rogaland Anorthosite Province. Norges Geologiske Undersøkelse Special Publication* **9**, 116–134.

Scoates, J. S. & Chamberlain, K. R. (1997). Orogenic to post-orogenic origin for the 1·76 Ga Horse Creek anorthosite complex, Wyoming, USA. *Journal of Geology* **105**, 331–343.

Smith, J. V. & Ribbe, P. H. (1969). Atomic movements in plagioclase feldspars: Kinetic interpretation. *Contributions to Mineralogy and Petrology* **21**, 157–202.

Smithson, S. B. & Ramberg, I. B. (1979). Gravity interpretation of the Egersund anorthosite complex, Norway: Its petrological and geothermal significance. *Geological Society of America Bulletin* **90**, 199–204.

Toplis, M. J. & Corgne, A. (2002). An experimental study of element partitioning between magnetite, clinopyroxene and iron-bearing silicate liquids with particular emphasis on vanadium. *Contributions to Mineralogy and Petrology* **144**, 22–37.

Vander Auwera, J. & Longhi, J. (1994). Experimental study of a jotunite (hypersthene monzodiorite): constraints on the parent magma composition and crystallization conditions (*P*, *T*, f_{O2}) of the Bjerkreim–Sokndal layered intrusion (Norway). *Contributions to Mineralogy and Petrology* **118**, 60–78.

Vander Auwera, J., Longhi, J. & Duchesne, J. C. (1998). A liquid line of descent of the jotunite (hypersthene monzodiorite) suite. *Journal of Petrology* **39**, 439–468.

Vander Auwera, J., Longhi, J. & Duchesne, J. C. (2000). The effect of pressure on D_{Sr} (plag/melt) and D_{Cr} (opx/melt): implications for anorthosite petrogenesis. *Earth and Planetary Science Letters* **178**, 303–314.

Westphal, M., Schumacher, J. C. & Boschert, S. (2003). High-temperature metamorphism and the role of magmatic heat sources at the Rogaland Anorthosite Complex in Southwestern Norway. *Journal of Petrology* **44**, 1145–1162.

Wiebe, R. A. (1992). Proterozoic anorthosite complexes. In: Condie, K. C. (ed.) *Proterozoic Crustal Evolution*. Amsterdam: Elsevier, pp. 215–262.

Wilmart, E. & Duchesne, J. C. (1987). Geothermobarometry of igneous and metamorphic rocks around the Ana–Sira anorthosite massif: implications for the depth of emplacement of the South Norwegian anorthosites. *Norsk Geologisk Tidsskrift* **67**, 185–196.

Xue, S. & Morse, S. A. (1994). Chemical characteristics of plagioclase and pyroxene megacrysts and their significance to the petrogenesis of the Nain anorthosites. *Geochimica et Cosmochimica Acta* **58**, 4317–4331.